This is a repository copy of *Forecast of the energetic electron environment of the radiation belts*.

AGU ADVANCING EARTH AND SPACE SCIENCE

Key Points:

- SNB³GEO electron flux forecasts are used to estimate the Nonlinear AutoRegressive Moving Average with eXogeneous outer boundary flux
- Two different of coupling mechanisms are investigated based on a fixed and Kp driven value of L^*_{GEO}
- For pastcasts of the March 2015 storm, the fixed L^*_{GEO} coupling shows better results than Kp driven coupling methodology

Correspondence to:

S. N. Walker,
simon.walker@sheffield.ac.uk

Forecast of the Energetic Electron Environment of the Radiation Belts

Simon N. Walker[1] , **Richard J. Boynton[1]** , **Yuri Y. Shprits[2,3,4]** , **Michael A. Balikhin[1]** , and **Alexander Y. Drozdov[3]**

[1]Automatic Control and Systems Engineering, University of Sheffield, Sheffield, UK, [2]Helmholtz Centre Potsdam, GFZ German Research Centre for Geosciences, Potsdam, Germany, [3]Department of Earth, Planetary, and Space Sciences, University of California, Los Angeles, CA, USA, [4]Institute of Physics and Astronomy, University of Potsdam, Potsdam, Germany

Abstract Different modeling methodologies possess different strengths and weakness. For instance, data based models may provide superior accuracy but have a limited spatial coverage while physics based models may provide lower accuracy but provide greater spatial coverage. This study investigates the coupling of a data based model of the electron fluxes at geostationary orbit (GEO) with a numerical model of the radiation belt region to improve the resulting forecasts/pastcasts of electron fluxes over the whole radiation belt region. In particular, two coupling methods are investigated. The first assumes an average value for L^* for GEO, namely $L^*_{GEO} = 6.2$. The second uses a value of L^* that varies with geomagnetic activity, quantified using the Kp index. As the terrestrial magnetic field responds to variations in geomagnetic activity, the value of L^* will vary for a specific location. In this coupling method, the value of L^* is calculated using the Kp driven Tsyganenko 89c magnetic field model for field line tracing. It is shown that this addition can result in changes in the initialization of the parameters at the Versatile Electron Radiation Belt model outer boundary. Model outputs are compared to Van Allen Probes MagEIS measurements of the electron fluxes in the inner magnetosphere for the March 2015 geomagnetic storm. It is found that the fixed L^*_{GEO} coupling method produces a more realistic forecast.

Plain Language Summary Significant increases in the number of energetic electrons within the radiation belts can pose a threat to satellites operating in the vicinity of geostationary orbit (GEO). Their existence can result in wide ranging effects from the disruption of operations to the complete loss of a satellite. Therefore, it is of vital importance to create accurate models for the forecast of the energetic electron environment. Generally speaking, there are two modeling methodologies used. One method creates highly accurate models from data, collected, for example, at GEO. Such models, however, are only valid in the region in which the measurements were made. The second uses simulations that, although less accurate than data-based models, are capable of tracking changes over large volumes of space. In this study, we investigate two methods for the coupling of a data-based and a numerical model to generate accurate forecasts of the electron dynamics within the whole inner magnetosphere. The first coupling method uses a set of fixed parameters to yield more realistic forecasts.

1. Introduction

Today accurate and timely forecasts of the high energy electron environment within the terrestrial radiation belts are used by industry to aid the operation, maintenance, and protection of spaced based assets that provide services such as communications and navigation (Baker et al., 2008; Green et al., 2017). The outer limits of the radiation belts lie in the region of geostationary orbit (GEO), an orbit that is very highly populated with commercial satellites that perform essential services to enable our modern way of life. The development of large fluxes of high energy electrons within the radiation belts can pose a threat to this essential infrastructure, causing anything from a temporary loss of service for a period of hours or weeks to the complete loss of satellites whose orbits traverse this region. The type of problem and its severity is dependant upon the energy of the incident particles. Electrons with energies of the order of ∼100 keV cause surface charging of the satellite body (Ganushkina et al., 2021). The resulting discharges may damage the outer skin and solar cells of a satellite. In contrast, higher energy electrons with energies of the order of MeV penetrate the satellite skin and deposit their energy within the internal subsystems of the satellite leading to discharges, memory upsets, or short circuits (Wrenn et al., 2002). The worst

scenarios can incur a substantial cost to activate hot spares or develop new, replacement hardware. Thus, it is necessary to provide forecasts that cover the whole of the radiation belt region.

Discovered in 1958 (Van Allen & Frank, 1959) the terrestrial radiation belts consist two regions of energetic protons and electrons that are trapped within the terrestrial dipole magnetic field. The outer belt, located at distances between 3 and 7 R_E, typically consists of highly energetic (0.1–10 MeV) electrons and high energy protons (1–100 keV) while the inner belt, between 1 and 3 R_E, is primarily composed of electrons with energies of several hundred keV and extremely high energy protons (several MeV) (e.g., Ripoll et al., 2020). The structure of the radiation belts is governed by the interplay of processes enabling particles to enter the radiation belts such as radial diffusion from the outer magnetosphere, sputtering of the atmosphere by cosmic rays, or injection from the plasma sheet or ring current as a result of geomagnetic activity and their energization and loss due to resonant interactions with localized plasma waves such as plasmaspheric hiss (e.g., Thorne et al., 1974), chorus (e.g., Horne & Thorne, 1998), and electromagnetic ion cyclotron (EMIC) waves (e.g., Lyons & Thorne, 1972; Y. Y. Shprits et al., 2006), resulting in a highly complex system. For instance, the occurrence of geomagnetic storms has been shown to increase (50%), decrease (25%), or to leave the fluxes of electrons unaffected (25%) (Reeves et al., 2003) while the acceleration of electrons to MeV levels requires the existence of two distinct electron populations (Jaynes et al., 2015). Thus, the modeling of the radiation belts is particularly challenging.

There are a number of models that have been developed to investigate and forecast the dynamics of the high energy electron populations in the vicinity of the radiation belts. These models can be divided into two broad classes. Data based models, as the name suggests, rely on the availability of large amounts of data to derive information regarding the dynamics of the electron fluxes based on solar wind measurements and geomagnetic indices. Often, depending upon the methodology employed, data derived models will provide excellent forecasts but tend to be opaque, sacrificing physical interpretation of the model at the expense of flexibility and accuracy (Coleman et al., 2018). Due to the requirement for large amounts of data, these models are usually restricted to the calculation of fluxes at GEO or low Earth orbit. The second class is physics based models. These models use first principles based physical processes such as radial diffusion and the energy and pitch angle scattering resulting from wave-particle interactions between the particles and plasma wave modes such as chorus, hiss, and EMIC waves. Table 1 provides a list of some of these models.

Previously, Roederer and Lejosne (2018) investigated the variation of $L*$ as a function of equatorial pitch angle and radial distance r for magnetic local time (MLT) of 0 and 12 hr and Kp values of 0 and 4, showing that $L*$ increases both as r increases and also with increasing geomagnetic activity. Konstantinidis and Sarris (2015) compared the calculations of $L*$ using the software models/libraries IRBEM-lib, LANL* (downloadable from http://www.lanlstar.lanl.gov/download.shtml) (Koller & Zaharia, 2011), SPENVIS (web interface https://www.spenvis.oma.be/) (Heynderickx et al., 2004), and ptr3D (Konstantinidis & Sarris, 2015). Their results showed that all four methods are in good agreement for quiet times and small values of r. However, their results did deviate with increasing initial pitch angles, distance, and geomagnetic activity.

In this report, we couple two of the models listed in Table 1, namely the electron flux forecasts at GEO resulting from the data based SNB³GEO models and the physics based Versatile Electron Radiation Belt model (VERB), taking advantage of the strengths of the different modeling techniques. The resulting VERB Nonlinear AutoRegressive Moving Average with eXogeneous (NARMAX) Coupled model (VNC) combines the highly accurate but spatially limited data based models of electron fluxes at GEO to set the boundary limits on the electron fluxes required for numerical simulations of the entire radiation belt region. Building on the initial work of Pakhotin et al (2014), this report compares two coupling methods, the first assuming a constant value of $L*$ for GEO while the second allows $L*$ to vary with geomagnetic activity level.

This paper is organized as follows. Section 2 provides a description of the two models. Section 3 outlines the two different approached to the coupling of the models while Sections 4 and 5 assess how the variation of the Kp index can affect the flux outer boundary conditions. An example of the fluxes calculated with the coupled models are presented in Section 6. Finally, Section 7 summarizes the results.

Table 1
Models for the Forecast of Electron Fluxes in the Vicinity of the Radiation Belts

Model name	Spatial extent	Reference
Data based models		
REFM (local linear predictors)	GEO	Baker et al. (1990)
SNB³GEO (NARMAX)	GEO	Boynton et al. (2016)
PreMevE (neural net)	$2.8 < L < 7$	Chen et al. (2019)
SHELLS (neural net)	$3 < L < 7$	Claudepierre and O'Brien (2020)
(neural net)	GEO	Fukata et al. (2002)
MERLIN (neural net)	Outer radiation belt	Smirnov et al. (2020)
Cross population coherence (empirical)	GEO	Shin et al. (2016)
Particle measurements (empirical)	GEO	Denton et al. (2016)
AE9, AP9, SPM (empirical)	LEO-GEO	Ginet et al. (2013)
Kalman filter (data assimilation)	$3 < L < 6$	Coleman et al. (2018)
VERB-DA-1D (data assimilation)	$1 < L^* < 7$	Y. Shprits et al. (2007)
DREAM—(data assimilation)	$3 < L^* < 10$	Reeves et al. (2012)
Physics based models		
RBE	$1 < L < 8$	Fok et al. (2008)
BAS-RBM	$2 < L^* < 7$	Glauert et al. (2014b)
VERB	$1 < L < 7$	Subbotin and Shprits (2009)
VERB 3D	$1 < L^* < 7$	Y. Shprits et al. (2013)
VERB-4D	$1 < L^* < 7$	Y. Y. Shprits et al. (2015)
Salammbô	$1 < L < 7$	Beutier and Boscher (1995)
		Varotsou et al. (2008)
DREAM-3D	$2.5 < L^* < 5.5$	Tu et al. (2013)

2. Model Descriptions

2.1. VERB

The motion of particles in the radiation belts may be divided into three components, namely particle gyration around the terrestrial field lines, the bouncing of the particle back and forth along the magnetic field between the mirror points, and the particle drift around the Earth due to the curvature and gradient of the terrestrial field. These three types of motion are characterized by different time scales or frequencies. For electrons, the cyclotron frequency is of the order 1–3 kHz while the bounce frequency is around 1–3 Hz and the drift frequency $0.001 < f < 100$ mHz depending upon particle energy and location within the radiation belt region (Schultz & Lanzerotti, 1974). These motions may be described in terms of a set of parameters, known as adiabatic invariants, that are conserved provided that changes in the particle motion occur on time/spatial scales larger than those associated with the above-mentioned types of motion. The first invariant is the magnetic moment of the particle as it gyrates around the field. The second invariant is related to the period of the particle as it bounces between magnetic mirror points while the third is related to drift of the particle around the Earth. While the assumption of invariance is only true for an ideal system, these invariant quantities provide a basic framework in which to study the dynamics of the radiation belts. The use of phase averaged fluxes enables the violation of the invariants to be expressed in terms of a diffusion equation with respect to each of the invariants. The violation of the different invariants may result from different physical processes such as the radial diffusion of particles or diffusion of the particles pitch angle or energy due to wave-particle interactions. These general diffusion equations, however, do not include terms for the systematic loss of energy from the system and so further terms are required to incorporate these effects. The resulting description of the evolution of the plasma distribution function is the Fokker-Planck equation (see Equation 1).

The global view of the Phase Space Density (PSD) of high energy (MeV) electrons presented in this report is simulated by the VERB numerical code (e.g., Subbotin & Shprits, 2009; Y. Y. Shprits, Subbotin, & Ni, 2009). VERB combines the radial diffusion equation for the violation of the third invariant (Dungey, 1965; Schultz & Lanzerotti, 1974) with the bounce-averaged diffusion equation, formulated in terms of equatorial pitch angle and momentum (Schultz & Lanzerotti, 1974) to quantify the violation of the first and second adiabatic invariants and hence describe the dynamical evolution of the plasma distribution function using the Fokker-Planck Equation 1. It incorporates the processes of radial diffusion, and the diffusion of particles in momentum, pitch angle, and mixed diffusion terms due to wave-particle interactions.

$$
\begin{aligned}
\frac{\partial f}{\partial t} = {}& L^{*2} \left.\frac{\partial}{\partial L^*}\right|_{\mu,J} \left(D_{L^*L^*} L^{*-2} \left.\frac{\partial f}{\partial L^*}\right|_{\mu,J} \right) \\
& + \frac{1}{p^2} \left.\frac{\partial}{\partial p}\right|_{y,L} \left(p^2 \langle D_{pp}(y,p) \rangle \left.\frac{\partial f}{\partial p}\right|_{y,L} + p^2 \langle D_{py}(y,p) \rangle \left.\frac{\partial f}{\partial p}\right|_{p,L} \right) \\
& + \frac{1}{T(y)y} \left.\frac{\partial}{\partial y}\right|_{p,L} \left(T(y)y \langle D_{yy}(y,p) \rangle \left.\frac{\partial f}{\partial y}\right|_{p,L} + T(y)y \langle D_{yp}(y,p) \rangle \left.\frac{\partial f}{\partial y}\right|_{y,L} \right) \\
& - \frac{f}{\tau}
\end{aligned}
\tag{1}
$$

where $y = \sin(\alpha)$, α being the equatorial pitch angle, p the particle momentum, $\langle D_{pp} \rangle$, $\langle D_{yp} \rangle$, and $\langle D_{yy} \rangle$ are the diffusion tensors averaged over MLT, and the particle bounce period, $T(y) = 1.3802 - 0.3198 \left(y + y^{1/2} \right)$ (Lenchek et al., 1961). The final term, f/τ, represents losses from the loss cone. τ is the characteristic electron lifetime and is assumed to be a quarter of the bounce time for particles within the loss cone and infinite for those outside (Subbotin et al., 2011).

In this study, the VERB code solves Equation 1 on a grid consisting of 31 linearly spaced bins in L^* covering the range $1 \leq L^* \leq 7$, 101 logarithmically spaced bins in energy between 0.01 and 10 MeV and 101 linearly spaced pitch angle bins in the range $0.3 \leq \alpha < = 89.7°$ with a time step of 0.2 hr, in line with that used previously by Pakhotin et al. (2014). The pitch angle boundary conditions (both upper and lower) are zero gradient in PSD for $0°$ and $90°$ equatorial pitch angle (Y. Y. Shprits, Chen, & Thorne, 2009). The energy diffusion operator assumes zero PSD at the upper energy boundary and a constant boundary condition at the lowest energy boundary. The variability of the upper boundary conditions in L^* are defined by the mapping of the NARMAX flux at GEO (see Section 2.2). This flux is used as a scaling factor for the PSD which is calculated using the average spectrum, obtained from observations (Y. Y. Shprits & Thorne, 2004; Y. Y. Shprits et al., 2006). The inner boundary for the simulation $f(L = 1) = 0$ is taken to represent loss to the atmosphere (Subbotin & Shprits, 2009). The constant lower energy boundary does not change in time. It is calculated using a steady state solution (radial profile) using the same spectrum as described above (at upper L boundary). It represents the balance of convective source and losses. The code is initialized by solving the steady state radial diffusion equation. VERB uses an implicit stepping scheme which has the advantage of not imposing limits on the time step and hence enables faster computation. Coefficients describing the process of radial diffusion are based on the electromagnetic parameterization of Brautigam and Albert (2000) while the wave-particle diffusion coefficients are computed from statistical studies of realistic wave parameters (W. Li et al., 2007) with wave normal angles taken Horne et al. (2005) (chorus) and Meredith et al. (2007) (hiss). Drozdov et al. (2015) and Drozdov et al. (2020) demonstrated that VERB can reproduce the dynamics of the ≤1 MeV electrons without EMIC waves, since EMIC waves primarily interact with higher energy electrons (Drozdov et al., 2017). For the scattering by the chorus at MeV energies, the strong diffusion limit (Kennel, 1969) is never reached (Y. Y. Shprits et al., 2008). The strong diffusion limit can only be reached if EMIC waves scatter particles (W. Li et al., 2007), however, these processes are usually effective at multi-MeV energies. Such high energies have not been included in these simulations. Further details of the diffusion coefficients used within VERB, together with the method to obtain flux boundary conditions for the radial diffusion operator may be found in Y. Y. Shprits, Subbotin, and Ni (2009). Within VERB, the plasmapause location is computed using the model of Carpenter and Anderson (1992) and the models of Sheeley et al. (2001) and Carpenter and Anderson (1992) are used for the density in order to compute the diffusion coefficients. More recent developments have extended the capabilities of VERB to include data assimilation techniques (Cervantes et al., 2020; Y. Shprits et al., 2007; Y. Shprits et al., 2013), allowing the numerical model to compare and correct its results based on observations by CRRES (Vampola, 1992) and Van Allen Probes (Stratton et al., 2013). The current study, however, does not employ these extended assimilation techniques.

2.2. SNB³GEO

The suite of models SNB³GEO (Boynton et al., 2015) for the modeling and forecasting of the fluxes of electrons with energies in the ranges >800 keV and >2 MeV were created using the NARMAX inputs methodology developed in the field of Systems Science to determine the output of a system as a function of the set of system inputs (Billings et al., 1989; Leontaritis & Billings, 1985a, 1985b). The NARMAX methodology has been applied in a wide range of multidisciplinary science and engineering fields including medicine, synthetic biology, modeling of financial systems, chemical reaction rates, and climate studies. In the field of space physics it has been used to model fluctuations in Dst (Boaghe et al., 2001) and Kp (Ayala-Solares et al., 2016), the evolution of shocklets in the foreshock (Coca et al., 2001), the determination of magnetospheric coupling functions (Boynton et al., 2011), and the forecast of electron fluxes at GEO (Balikhin et al., 2016; Boynton et al., 2013, 2015, 2016). It is the results of these latter models that are used in this study.

NARMAX models represent a large class of nonlinear models of which the widely known and used Volterra models are a special case. Equation 2 shows the general form of a NARMAX model.

$$y(t) = F[y(t-1), y(t-2), \ldots, u_1(t-1), u_1(t-2), \ldots, u_2(t-1), u_2(t-2), \ldots, \epsilon(t-1), \epsilon(t-2) \ldots .] \quad (2)$$

where y represents measurements of the system output, u_n the system inputs, and ϵ the error terms. The times t, (t−1), (t−2) … represent the lagged times tags of the various input and output parameters. The use of different lag values incorporates system history or memory effects into the model. F[.] is an unknown nonlinear function but which may be expressed as a set of polynomial, B-spline, or radial basis functions. The main advantages of NARMAX models in comparison with neural net based models is their transparency, ease of interpretation and comparison with first principles based physical models.

NARMAX is a three stage process. The first stage identifies the most significant model terms from the set of all combinations of the input and output parameters. This is an iterative process, determining the model term that has the greatest contribution to the variance of the output and then removing the effects of this term from the output signal within each iteration cycle, and terminating when either an appropriate number of terms have been found or the output signal consists of noise. If the output still contains a signal when the set of model terms have been identified it is indicative that the set of model input parameters is incomplete. In contrast, neural net based models will return a model in which the output of the system is based only on the system input parameters provided. The second stage of NARMAX estimates the coefficient of each of the selected model parameters. The third stage, model validation, is used to justify and test the model. A complete description of the NARMAX methodology may be found in Billings (2013).

The NARMAX methodology has been used to derive two separate models for the >800 keV and >2 MeV integral electron flux channels available from the GOES-13 EPAD instrument (Hanser, 2011). Measurements of fluxes at >800 keV began with GOES-13 when it replaced GOES-12 at the GOES East location (75°W) in 2010 and are available until 2020 while measurement of the fluxes >2 MeV began with GOES-6 and continue to this day (Boynton et al., 2015). Based on earlier studies by Balikhin et al. (2011) and Boynton et al. (2013) using daily averages of solar wind parameters and electron fluxes from the Los Alamos National Laboratory Synchronous Orbit Particle Analyzer instruments (Reeves et al., 2011) it was determined that the most influential solar wind parameters on the evolution of the electron fluxes at GEO were the density or velocity, depending on the energy of electrons considered. The NARMAX models used in the current study for the forecast of electron fluxes at GEO were trained using daily averages of the solar wind velocity, density, Z component of the Interplanetary Magnetic Field (IMF), Dst index, and the fraction of the day during which the solar wind was southward (from the OMNI data set) as input to the model. The system outputs were the daily averaged electron fluxes measured by the GOES 13 westward facing sensor head for the >800 keV electron flux model and GOES 10, GOES 11, and GOES 12 for the model of >2 MeV fluxes (Boynton et al., 2016). Both models were validated using data from the GOES 13 westward facing sensor. The output from these models is a forecast for the daily averaged electron flux at GEO. These NARMAX models have proven to be highly successful. Their results compare well with measured values of the fluxes (Boynton et al., 2015) with prediction efficiencies of around 0.70 and 0.79 and correlation coefficients of 0.84 and 0.89 for the >800 keV and >2 MeV flux channels respectively. Their performance has been shown to be slightly better than other models such as the Relativistic Electron Forecast Model (Baker et al., 1990) at NOAA (https://www.swpc.noaa.gov/products/relativistic-electron-forecast-model) (Balikhin et al., 2016). The current suite of NARMAX models is capable of producing good forecasts for changes in the flux levels that

Table 2
Potential Sources for Current and Forecast Values of the Kp Index

Method used	Source address	Model reference
Artificial Neural Network	https://www.spaceweather.se	Boberg et al. (2000)
		Wintoft et al. (2017)
	https://services.swpc.noaa.gov/text/3-day-forecast.txt	Wing et al. (2005)
NARMAX	http://www.ssg.group.shef.ac.uk/USSW2/Kp/	Ayala-Solares et al. (2016)

occur on time scales of a days due to the use of daily flux averages for the output parameter. However, in order to account for flux changes on shorter time scales, such as those observed during magnetopause shadowing events, it would be necessary to include models to forecast such events (e.g., Glauert et al., 2014a; Herrera et al., 2016) and to increase the time resolution of the models. It has been shown by (Meredith et al., 2015) that the flux of >2 MeV electrons measured at the GOES West location is typically higher (by a factor of 2.5) than that measured at the GOES East location. These authors attribute this difference to the difference in L-shell between the two measurement locations. Thus, the NARMAX models only forecast the expected fluxes at the distance of the GOES East location.

These forecasts are only applicable to GEO, the reason being that the NARMAX modeling methodology is data driven and there is only sufficient data coverage at GEO. As a result, they can provide no information about the fluxes of electrons for regions either outside or inside GEO. In order to expand the forecasts to encompass the spatial variation of the electron distribution throughout the radiation belt region, the output from these models is used to estimate the electron boundary flux required by VERB.

This report investigates the coupling between VERB and NARMAX. It was previously mentioned that the NARMAX model electron flux estimates from SNB^{3}GEO are only applicable in the vicinity of GEO, that is, at a radial distance of $L = 6.6$ (where L is the McIlwain L parameter [McIlwain, 1961]). However, numerical codes, such as VERB, solve the Fokker-Planck Equation 1 using a spatial grid based on the parameter L^* (Roederer, 1970). L^* is inversely proportional to the third adiabatic invariant and describes the location of the drift path of an electron with a pitch angle α as it propagates around the Earth. Thus, while the L^* location of an electron drift orbit is constant, its radial distance (measured in terms of, say, the McIlwain L-parameter) will vary. Unless specified otherwise, all values of L^* presented in this report were computed assuming an electron pitch angle $\alpha = 90°$. In addition, the radial distance expressed in L^* is also dependant upon geomagnetic activity. In this paper, two different methods for the mapping of electron fluxes measured/forecast at $L = 6.6$ to the VERB outer boundary at $L^* = 7$ are investigated and compared. The first assumes that the location of GEO as a function of L^* is independent of geomagnetic activity and always situated at a radial distance of $L^*_{GEO} = 6.2$. In the second, estimates of the actual average value for L^*_{GEO} are based on the Tsyganeko T89c model of the geomagnetic field (Tsyganenko, 1989). This model takes into account the level of geomagnetic activity as expressed by the Kp index.

3. Methodology

VERB uses two input parameters. The first is Kp to indicate the level of geomagnetic activity. VNC has been configured to use both the definitive/provisional values for Kp that are available from the German Research Centre for Geosciences (GFZ) as well as forecast values. For the purposes of this study, forecast values for the Kp index were generated by the Sheffield NARMAX model (Ayala-Solares et al., 2016). Table 2 lists potential sources for such forecasts.

The second input is a scaling value B_f that is used to adjust the average GOES flux values at the outer boundary ($L^* = 7$). Using the SNB^{3}GEO models for the forecast of electron fluxes corresponding to the GOES integral flux channels of >800 keV and >2 MeV it is possible to estimate (assuming a Maxwellian distribution) the differential flux of electrons at any suitable energy (see Section 5). In the present study, an energy of 0.892 MeV was used since it enables a direct comparison with one of the MagEIS energy channels. This flux is then propagated to the location of the VERB outer boundary (details are shown in Appendix B) and compared to the GOES average fluxes used within VERB (see Table 2 of Y. Y. Shprits, Subbotin, & Ni, 2009) and hence to derive the scaling
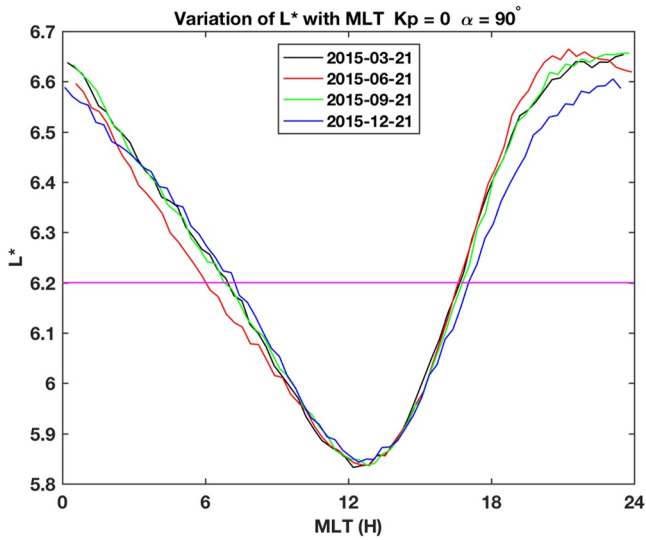
Figure 1. The variation of L^*_{GEO} as a function of magnetic local time for the equinox and solstice dates in 2015 for a value of Kp = 0 and pitch angle $\alpha = 90°$.

factor B_f (Subbotin et al., 2011). The loss terms and diffusion coefficients (Brautigam & Albert, 2000) determined by VERB are both parameterized by Kp. The solution of the radial diffusion equation with df/dt = 0 provides the radial PSD profile. These PSD values are then scaled by the factor B_f. This method (Subbotin et al., 2011) may be used to determine the steady state profile for the PSD for fixed values of either μ and J or μ and K.

The L^* position of GEO varies depending upon MLT and the level of geomagnetic activity. The determination of L^* at a particular location requires a realistic model for the terrestrial field. In this study, the T89c (Tsyganenko, 1989) model is used for field line tracing. This model uses the Kp index to characterize the shape of the terrestrial field based on the level of geomagnetic activity. Determination of L^* is calculated using MATLAB routines from the publicly available IRBEM-lib library of source codes (Bourdarie & O'Brien, 2009) (https://craterre.onera.fr/prbem/irbem/description.html). The electron boundary flux is estimated using results from the NARMAX forecasting models which is then propagated from the L^* position of GEO, estimated at 6.2 for the initial parts of this work, to the VERB outer boundary at $L^* = 7$.

In all runs model discussed in this report the VERB code was configured to include radial, pitch angle, energy, and mixed diffusion terms that account for the effects of chorus and hiss waves, together with parameterizations for the plasmapause location. This configuration is identical to that used in the previous study by Pakhotin et al. (2014).

4. Variation of L^* With Time and Geomagnetic Activity

In the initial study by Pakhotin et al. (2014) the coupling between the SNB³GEO models and VERB assumes a fixed value for GEO in terms of L^* that is, GEO is located at $L^*_{GEO} = 6.2$ and that this value does not change regardless of time of day, time of year, or geomagnetic activity level. This section investigates how the value of L^*_{GEO} varies with time and geomagnetic activity.
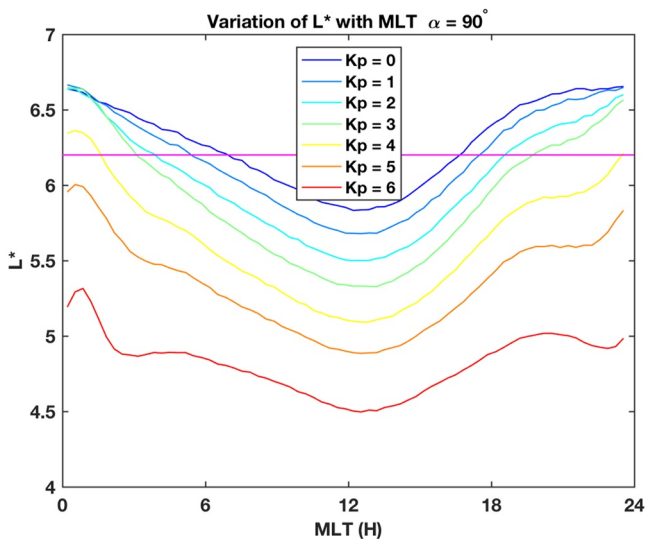

Figure 2. The variation of the L^*_{GEO} as a function of magnetic local time for the values of Kp in the range 0–6 at the vernal equinox, 21 March 2015 and a pitch angle $\alpha = 90°$. The magenta line represents the value of L^* used in the fixed coupling methodology.

The spatial variation of L^*_{GEO} of GEO (assumed to be a circular orbit of radius 42,165 km and zero inclination) is shown in Figure 1 for a constant value of Kp = 0 and assuming a particle pitch angle $\alpha = 90°$. The black, red, green, and blue traces correspond to the spring equinox, summer solstice, autumn equinox and winter solstice respectively. All traces exhibit a similar shape, varying between $L^* \sim 5.8$ around midday and between $L^* \sim 6.6$–6.7 at midnight. The horizontal magenta line marks $L^* = 6.2$, the value used in the first method of coupling. The average value of L^* on each of the dates varies between 6.24 and 6.26 and is in line with the fixed value of L^*_{GEO} used in the first coupling method. Results for Kp = 1 and 2 show average values of L^*_{GEO} are 6.1 and 6.0 respectively. Thus, for typical low values of Kp, this assumption holds quite well.

As the Kp index increases to values of 3 and higher this assumption is no-longer true. The variation of L^*_{GEO} for Kp values in the range 0–6 at the vernal equinox is shown in Figure 2. Again, the magenta line represents $L^*_{GEO} = 6.2$. The L^* value of GEO is seen to move to lower values of L^* with increasing Kp. Average values for L^*_{GEO} are around 6.1, 5.9, 5.3, and 4.8 for Kp values of 1, 3, 5, and 6 respectively. Thus, changes in geomagnetic activity (as expressed using the Kp index) have a significant effect upon the average value of L^*_{GEO}.

It was noted from Figure 1 that for Kp = 0 the radial distance of L^*_{GEO} is similar at different times of the year. However, this is not the case for higher
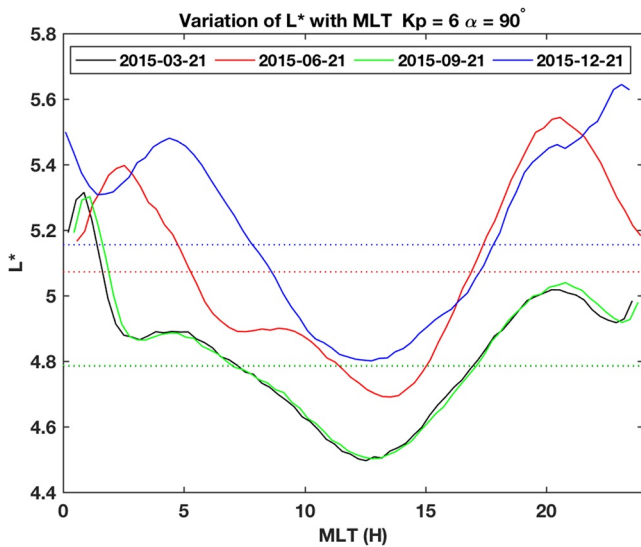
Figure 3. Variation of the L_{GEO}^* at different times of the year, with a high value of Kp = 6.

values of Kp. Figure 3 shows the variation of L_{GEO}^* with MLT when Kp = 6 for times around the spring (black) and autumn (green) equinoxes and the summer (red) and winter (blue) solstices. The dotted lines represent the average value of L^* for each date. It is clearly seen that the values of L^* around the equinoxes are very similar, in the range $4.5 < L^* < 5.3$, with an average of the order of 4.8. The solstice values, however, are quite different in profile. Around the summer solstice the location of GEO varies in the range $4.7 < L^* < 5.4$ averaging a value of around $L^* \sim 5.1$. The winter solstice date shows a variation in the range $4.8 < L^* < 5.6$ averaging around $L^* \sim 5.2$. This change reflects the changes in orientation of GEO with respect to the terrestrial magnetic field. At the equinoxes, the geomagnetic dipole axis is oriented on average perpendicular to the sun vector, hence the similarity between the profiles of L^*. However, at the solstices the field orientations are substantially different, depending on whether the dipole axis points toward or away from the sun direction.

5. Changes in Flux Levels

Figures 1–3 demonstrate that the radial location of GEO, expressed in terms of L^*, can change significantly as a function of both the time of year and the level of geomagnetic activity. In this section the effects of this change on the electron flux levels at the VERB outer boundary are investigated.

The typical ranges of fluxes forecast by the SNB³GEO models are 1×10^3–5×10^5 cm^{-2} sr^{-1} s^{-1} and 1–600 cm^{-2} sr^{-1} s^{-1} for the >800 keV and >2 MeV integral channels respectively. The resulting estimates of the differential flux at 0.892 MeV lie in the range 0.6–2×10^3 cm^{-2} sr^{-1} s^{-1} at GEO.

In the previous section, it was shown that the value of L^* for GEO can vary in the range $4.5 < L^* < 7$ for moderate values of Kp. Figure 4 displays the variation in the computed electron fluxes at $L^* = 7$ based on the flux at GEO as a function of the value of L^* for GEO assuming $4.5 < L_{GEO}^* < 7$. The colors represent initial differential flux levels of 0.892 MeV electrons at GEO of 0.1 (black), 1 (red), 10 (green), 100 (blue), and 1,000 (cyan) cm^{-2} sr^{-1} s^{-1}.

From Figure 4 it can be seen that the VERB outer boundary electron fluxes can vary by a factor of ≈ 4 as the value of L_{GEO}^* varies between 4.5 and 7. These changes may have a significant effect on the output electron energy spectra resulting from the VERB simulation.

6. Example Simulations

In the previous sections, the effects of modifying L_{GEO}^* have been investigated. It was shown that as the level of geomagnetic activity increases the assumption that on average GEO lies at $L_{GEO}^* = 6.2$ is no longer appropriate. Thus, in order to improve the forecasts of the electron distributions from VERB it may be necessary to modify L^* based on the current value of Kp. In this section we compare the results from two VNC simulations using a fixed and Kp driven values for the electron outer boundary flux with measurements from the Van Allen Probes A MagEIS instrument (Blake et al., 2013). Two time periods are considered. The first corresponds to a prolonged period of low Kp, the second to the St. Patrick's Day storm of 2015.

6.1. Quiet Period

The first period modeled using the VNC model covers the period 2014-06-20 to 2014-08-12. During this period, the maximum of the Kp index was 3⁺. This limiting value for Kp was chosen to ensure a long period
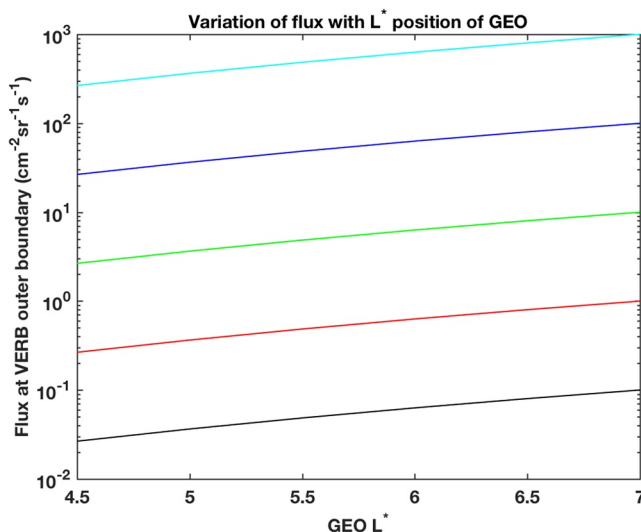

Figure 4. The propagated electron flux at $L^* = 7$ as a function of the changing value for L_{GEO}^*. The fluxes measured/forecast at geostationary orbit are 0.1 (black), 1 (red), 10 (green), 100 (blue), and 1,000 (cyan) cm^{-2} sr^{-1} s^{-1}.
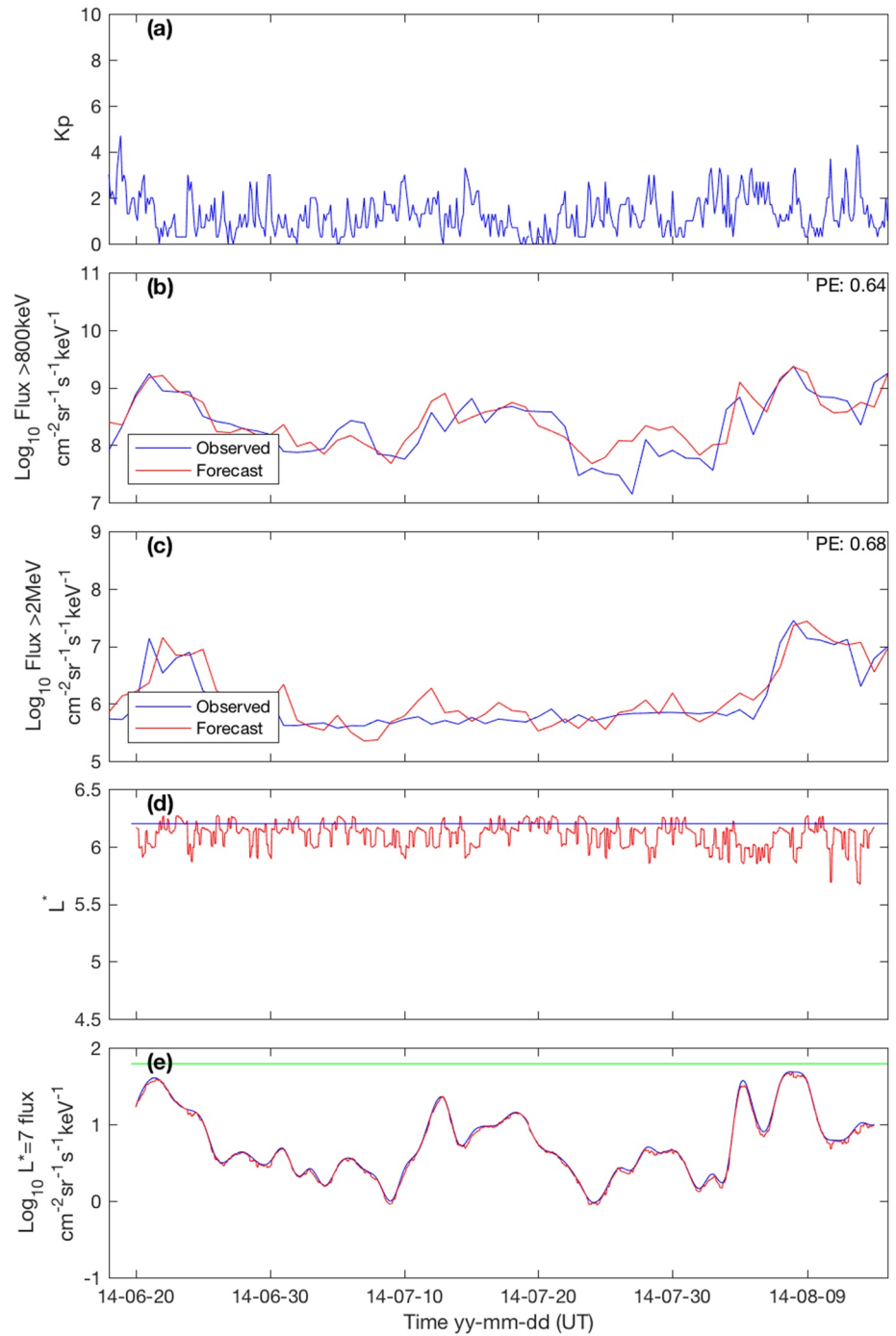
Figure 5. Variation of input values to the Versatile Electron Radiation Belt Nonlinear AutoRegressive Moving Average with eXogeneous (NARMAX) Coupled model. Panel (a) shows measured values for the Kp index. Panels (b and c) compare measurements of the geostationary orbit electron fluxes (blue) with NARMAX model forecasts (red) for the energy channels $E > 800$ keV and $E > 2$ MeV respectively. The variation of L^*_{GEO} is shown in Panel (d) for the fixed L^* (blue) and variable L^* (red) coupling methods while Panel (e) displays the flux of 0.892 MeV electrons at the Versatile Electron Radiation Belt model outer boundary for the fixed (blue) and Kp driven (red) coupling methodologies. The green curve represents the average value of the GOES flux at this energy.

(54 days) during relatively quiet geomagnetic conditions occurred. Figure 5 shows the parameters used for input to the VNC model during this period. Panel (a) shows the variation of the measured Kp index. As can be seen, typically Kp < 3 and no storms were identified. Unfortunately, forecast Kp data from the Sheffield NARMAX

model are currently only available after 2015. Thus, for this simulation, the Kp values used are those measured and archived at GFZ. Panels (b) and (c) show the GEO fluxes measured by the >800 keV and >2 MeV electron detector channels on GOES 13 (Hanser, 2011) (blue curves) together with forecasts of the fluxes from the University of Sheffield NARMAX based models (Boynton et al., 2015) (red curves). For the majority of this period, the forecasted and measured flux levels are very similar. The quality of these forecasts are assessed using estimates of the prediction efficiency (PE) metric, defined as 1—mean square residual divided by variance of data (see Equation 3). This has been used in numerous previous studies (e.g., Nagai, 1988; Rastätter et al., 2013; Temerin & Li, 2006).

$$PE = 1 - \frac{\Sigma(y-x)^2}{\Sigma(y-\hat{y})^2} \qquad (3)$$

where y is the measured data series with average $\hat{y}$ and x is the forecast data series. A value PE = 1 implies perfect prediction, zero implies that the average of the predicted values is equal to the average of the measured data set. A positive value, therefore, shows that model predicted variations are better than using a constant flux while negative values indicate that the model is worse. The PE for the electron fluxes in the >800 keV and >2 MeV energy channels are 0.64 and 0.68 respectively. These prediction efficiencies are similar those reported by (Glauert et al., 2021) using SaRIF forecast system that is based on the BAS-RBM description of electron fluxes in the radiation belts. Panel (d) displays the location of GEO as expressed by L^*. The blue curve represents the value $L^*_{GEO} = 6.2$, the value used in the fixed L^* coupling method. The red curve shows the variation of L^*_{GEO} when L^* is allowed to vary depending upon Kp. Throughout the majority of the period being studied the variable coupling method yields a value for L^*_{GEO} in the range 6.0–6.3, which is very similar to that assumed in the fixed L^*_{GEO} coupling method in which $L^*_{GEO} = 6.2$. Panel (e) shows the estimated electron fluxes at the VERB outer boundary at $L^* = 7$. The blue curve results from using the fixed L^*_{GEO} coupling methodology where as the red curve indicates the flux calculated assuming a Kp driven variation in L^*_{GEO}. The green line represents the initial flux value, derived from GOES data, that is built in to VERB (Y. Y. Shprits, Subbotin, & Ni, 2009). As expected, there is little difference in the flux level between the two coupling methods.

Despite the fact that Kp < 3 for the majority of this period, the variation in the observed and forecasted fluxes of electrons in the two energy channels is around one order of magnitude. There are three periods that exhibit increased fluxes. The first it at the start of the period under investigation when Kp values of 4 and 4⁺ were observed, and the fluxes in both energy channels showed an increase maximizing at around 09:00 UT on 21 June. The second increase, between 16:00 UT on 10 July and 04:00 UT on 23 July, is clearly visible in the >800 keV channel while the fluxes of >2 MeV electrons remain constant. The final increase in the fluxes occurs around 22:30 UT on 1 August for the >800 keV channel while increases in the >2 MeV electrons begin about 5 days later. These peaks in the flux levels result in increases in the estimated electron flux at the VERB outer boundary location at $L^* = 7$ (panel e). These flux increases occur during periods when Kp = 3 or above.

The results of the simulation of this period are shown in Figure 6. Panel (a) shows the Kp index for reference. Panels (b) and (c) show the variation of the 0.892 MeV fluxes at a pitch angle of 90° as a function of time and L^* using the fixed (panel b) and variable (panel c) coupling methods while panel (d) flux measurements from the MagEIS instrument (energy 0.909 MeV, pitchangle 90°). Panel (e) shows a comparison of the electron fluxes at a location $L^* = 5.4$ resulting from the simulations using fixed L^* coupling (blue), variable coupling (red) and MagEIS measurements (green).

The changes in the fluxes observed by GOES 13 at GEO (Figure 5) are observed by the Van Allen Probes (Figure 6 panel d) and, to a lesser extent, in both simulations of this event. It is clear from Figure 6 panel (e) that while the averaged measured fluxes at $L^* = 5.4$ vary continuously during this period, those forecast by the models show a much smaller variation and also lag behind the observed changes by around a day or more. This lag is most probably the result of the NARMAX model that was generated using daily flux averages which tend to average out any changes in the flux levels that occur on time scales of less than a day. These results also show that the use of the fixed, $L^*_{GEO} = 6.2$ tends to result in higher fluxes than those resulting from the Kp driven coupling method. Neither coupling methodology produces consistently better forecasts. Estimates of the PE, calculated for various intervals during the period of interest, are shown in Table 3. If the whole period is considered, then the fixed coupling method produces the best results where as for periods in which the fluxes remain low the variable coupling method is marginally better.
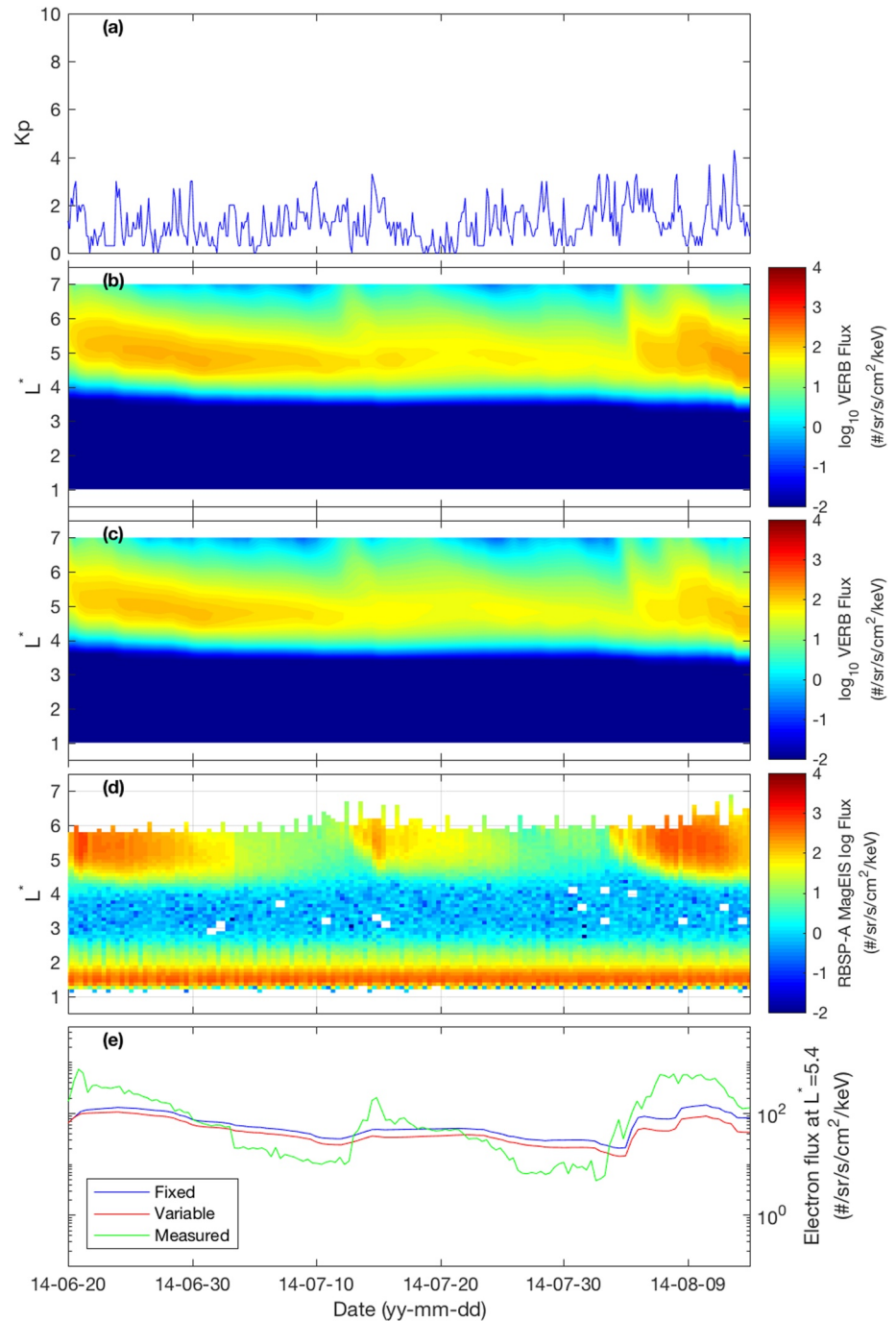
Figure 6. A comparison of Versatile Electron Radiation Belt model (VERB) simulations and measurements from the Van Allen Probes A MagEIS instrument. Panel (a) shows the Kp index for reference. Panels (b and c) show the variation of fluxes of ~900 keV electrons with L^* from VERB assuming a constant $L^*_{GEO} = 6.2$ (panel b) and Kp driven L^*_{GEO} (panel c). Panel (d) shows MagEIS measurements of 900 keV electrons for comparison. Panel (e) compares cuts through the fluxes shown in panels (b–d) at $L^* = 5.4$.

6.2. Storm Period

The St. Patrick's Day storm of 2015 (see special issue of Journal of Geophysical Research (Space Physics) Zhang et al., 2017) was the first geomagnetic storm of solar cycle 24 during which Dst was less than 200 nT (Wu et al., 2016). It was caused by the interaction of a coronal mass ejection (CME) with the terrestrial magnetosphere. A C9 class solar flare erupted from the solar surface at around 02 UT on 15 March, appearing as a partial halo

Table 3
Prediction Efficiencies of the Electron Flux at L* = 5.4

Time period	Fixed coupling	Variable coupling
Quiet period		
2014-06-20–2014-08-14	0.12	−0.07
Storm period		
2015-03-08–2015-03-19	−0.10	−0.50

CME in SOHO LASCO/C2 observations (Wu et al., 2016). Wind observed the passage of an interplanetary shock just 56.13 hr later and a Sudden Storm Commencement was observed at 04:45 on 17 March. At 10 UT the IMF turned southward and Dst dropped to −80 nT for a short while after which a short respite occurred as the field returned northwards. A few hours later, the IMF turned southward again due to the field within the magnetic cloud and the storm intensified, with Dst dropping to −223 nT and compressing the magnetopause to around 6.1 R_E (Goldstein et al., 2017).

Figure 7 shows the variation of the input parameters to the VNC model in the period 26 February–2 April 2015 using the same format as Figure 5. Panel (a) shows the Kp index. The blue curve corresponds to the values of the Kp index available from GFZ while the red curve is the output of a NARMAX based model for the evolution of Kp (Ayala-Solares et al., 2016). As can be seen, the correspondence between the GFZ measurements and model output is good, with a PE of 0.75 for the period being investigated. At the beginning of this period, Kp is low, typically in the range 0 < Kp < 3, indicating geomagnetically quiet conditions except for two deviations on 1 and 2 March when the level of geomagnetic activity a level indicating the occurrence of minor geomagnetic storms (Kp ∼ 5). On 17 March Kp suddenly increases to Kp = 8⁻, evidence for a strong to severe level geomagnetic storm initiated by a CME that erupted from the surface of the Sun 2 days before. When this CME struck the terrestrial magnetosphere it would have compressed the dayside such that the magnetopause moved inwards, encountering the radiation belts. This change in the shape of the terrestrial field would lead to a change in the average L^* position of GEO. The fluxes of electrons measured by the GOES 13 electron spectrometers (blue curves) together with forecasts of the fluxes from the NARMAX based models (red curves) are shown in Panels (b) and (c) corresponding to the >800 keV and >2 MeV integral electron flux channels respectively. These panels show the high correlation between measurements and model forecasts, with prediction efficiencies of 0.77 for the >800 keV channel and 0.81 for the >2 MeV channel. It is noticeable that the prediction efficiencies for the disturbed data set are higher than those of the quiet time data set. This may probably result from a combination of the facts that the data set used for the quiet time PE is longer than that for the disturbed case and that the probability distribution of the residuals with respect to the respective mean values has wider shoulders in the case of the quiet data set where as data set for the disturbed case is generally narrower but exhibits a small number of outliers. Both energy channels exhibit dips in the electron fluxes corresponding to periods of high Kp, indicating a loss of electrons from the radiation belts in the vicinity of GEO. Panel (d) displays the location of GEO as expressed by L^*. The blue curve represents the value L^*_{GEO} = 6.2, the value used in the fixed L^* coupling method. The red curve shows the variation of L^*_{GEO} when L^* is allowed to vary depending upon Kp. It is clear that, except for the period 9–11 March, the value of L^*_{GEO} is overestimated. In the quiet periods before the main storm L^*_{GEO} is typically in the range 5.8–6.1, not too different from the assumed value used in the fixed coupling method and so the initial coupling model that assumed GEO to be at a distance of $L^* \sim 6.2$ would be expected to yield reasonable results. However, during the minor and severe storm periods the value of L^*_{GEO} drops to 5.3 and 4.8 respectively, a substantial deviation from the assumed constant value. Finally, Panel (e) shows the resulting electron fluxes at the VERB outer boundary at L^* = 7. The blue curve results from using the fixed L^*_{GEO} coupling methodology where as the red curve indicates the flux calculated assuming a Kp driven variation in L^*_{GEO}. For the majority of the period studied, these boundary flux levels are very similar with the ratio of the fluxes $J_{fixed}/J_{variable} \sim 1.1$ where as this ratio increases to ∼1.6 for the minor storm periods and ∼2.1 during the severe storm period. Thus, during the storm periods, the increase in Kp is associated with a reduction in the value of L^*_{GEO}, leading to a reduction in the level of flux at the VERB outer boundary. The green line indicates the flux level used within VERB to define the outer boundary condition for the radial diffusion operator. This value is compared to the value of the flux propagated from GEO to yield the boundary flux factor B_f that is used by VERB to scale the outer boundary flux values at all energies.

Figure 8 shows the comparison of the simulations and observations for the storm period in the same format as Figure 6. Panel (a) displays the values of Kp for reference. Panels (b) and (c) show the results of the two VERB simulations using fixed and variable values of L^*_{GEO} to determine the outer boundary electron fluxes respectively. Panel (d) shows the orbit averaged electron measurements from the MagEIS instrument onboard Van Allen Probe A. Panel (e) compares the fluxes from the models and observations. The simulation period for this event began on 1 March 2015, using the input data shown in Figure 7, but the results during the initial period 1–7 March were not used in any subsequent analysis. In the period 9–17 March (i.e., before the storm) both simulations show a similar
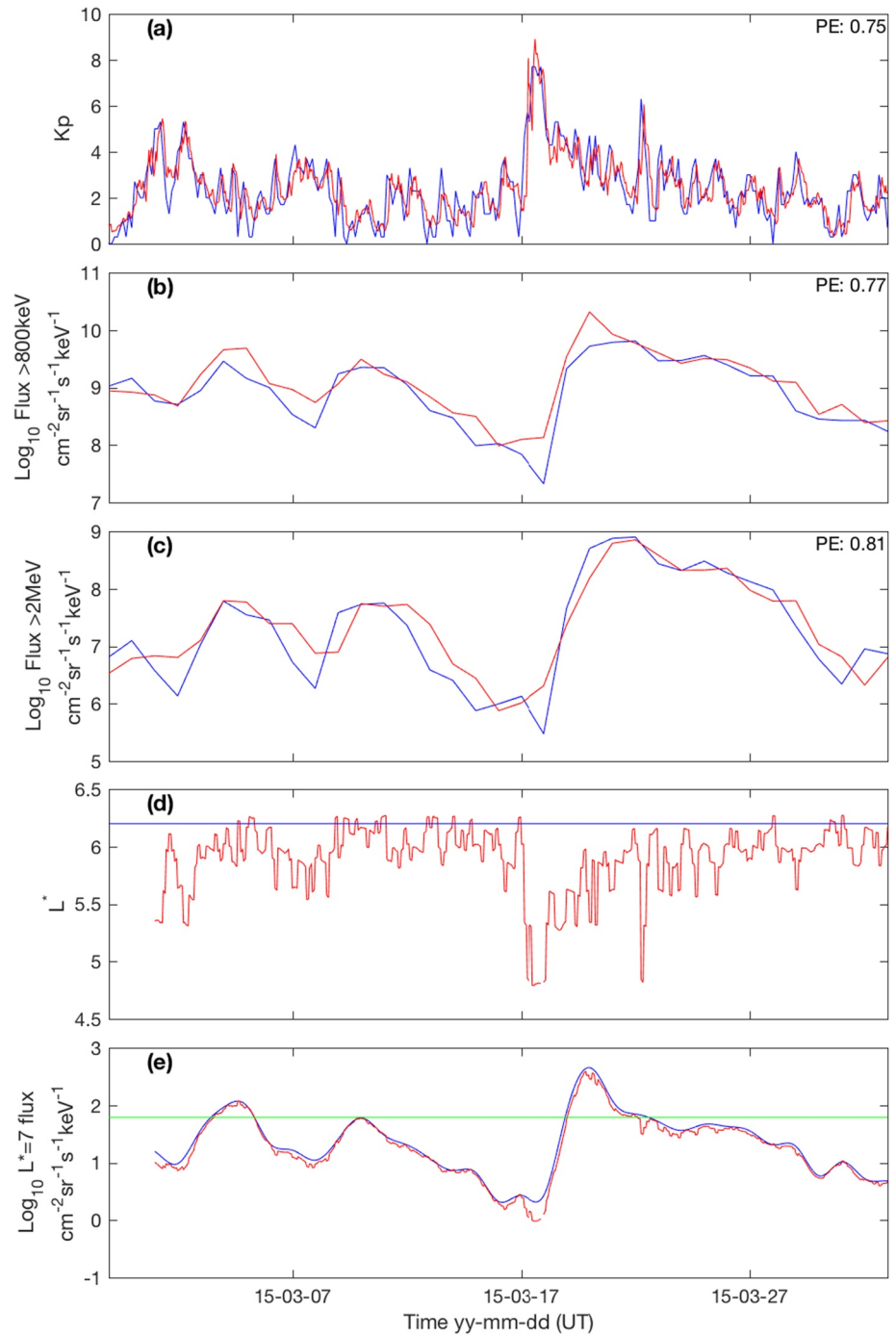
Figure 7. Variation of input values to the Versatile Electron Radiation Belt ARMAX Coupled model using the same format as Figure 5.

radial profile of electrons with a peak in the distribution occurring just inside $L^* = 5$. The similarity of these two sections of the simulations indicate that at low geomagnetic activity levels, the change in L^*_{GEO} is minimal and has little effect on the final simulations. On closer inspection it appears that the fluxes estimated using the fixed $L^*_{GEO} = 6.2$ are slightly higher than those using the Kp driven variable L^*_{GEO}. This reflects the fact that for Kp > 2 the estimated boundary flux values are very slightly less in the Kp driven case. In comparison to actual measurements from the Van Allen Probes A MagEIS instrument (panel c) both simulations show smaller and narrower peaks in the radial particle profile which may indicate that some processes are operating that were not flly
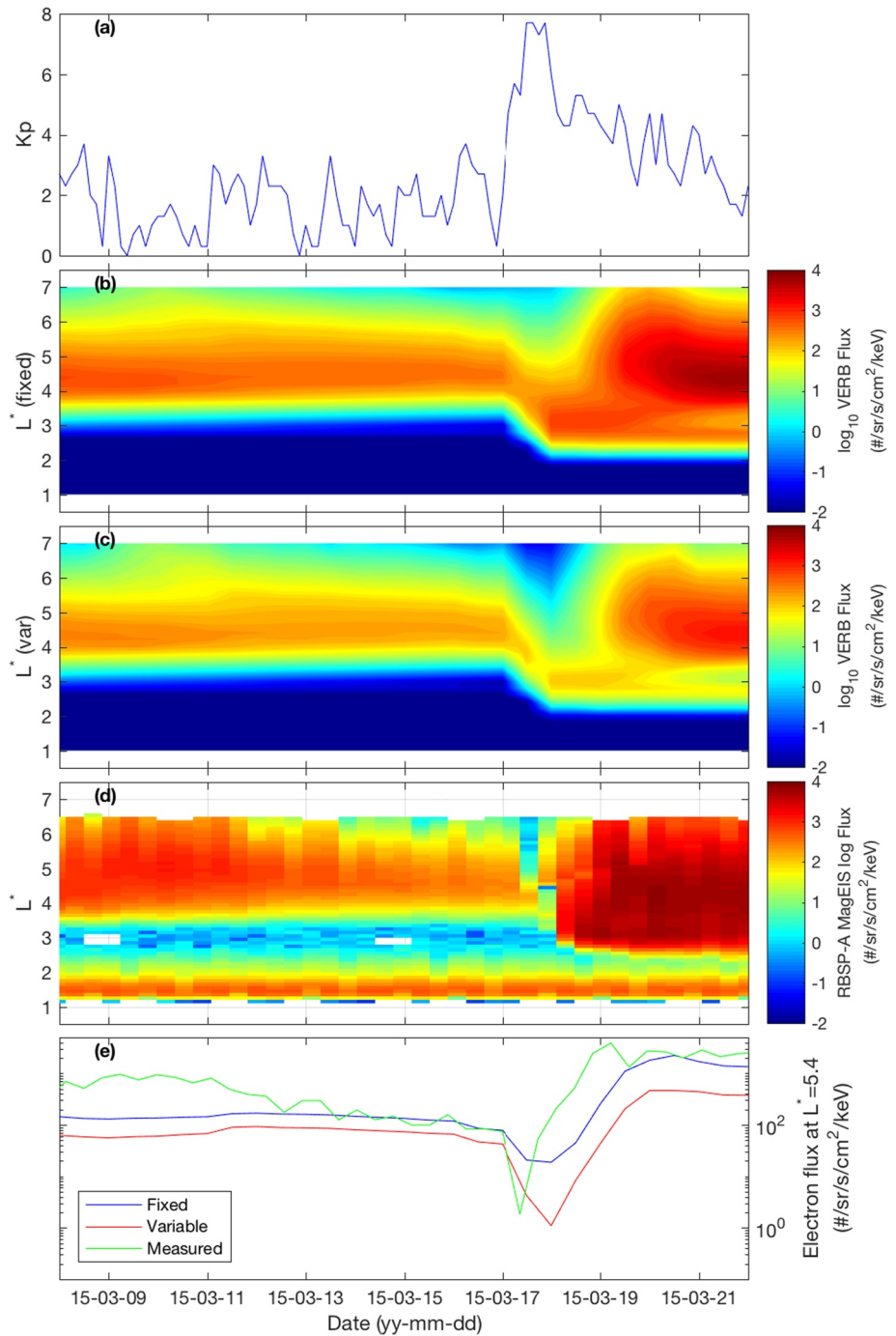
Figure 8. A comparison of Versatile Electron Radiation Belt model simulations and measurements from the Van Allen Probes A MagEIS instrument using the same format as Figure 6.

accounted for within the VERB runs. It has been shown by Allison and Shprits (2020) and Allison et al. (2021) that plasma density is an important factor for the local acceleration, especially when the density is low (W. Li et al., 2014). During this event the density was indeed lower than the statistical value and so is expected to affect local particle acceleration processes. At just after midday on 17 March a CME struck the terrestrial magnetosphere. At this time the value of Kp rises to around 8^-. From Panel (e) of Figure 7 it is clear that this change in Kp causes a large change in the VERB outer boundary electron flux. At this point, the results of the two VERB simulations begin to differ significantly. Both show a depletion of particles, first at higher L^* and then at lower

occurring over a period of 1 day. This process is also observed in the actual observations but occurs a great deal faster in only a few hours. This rapid loss of the electron population is a result of magnetopause shadowing caused by the sudden compression of the magnetopause, moving the boundary inwards into the radiation belt region. As the magnetopause intersects the magnetic field lines of the radiation belt region, the electron populations, initially located on closed drift shells suddenly find themselves on open magnetic field lines and are lost from the system. These losses can occur due to two mechanisms (Staples et al., 2022), such as direct loss (e.g., Green et al., 2004; X. Li et al., 1997) or as a result of the subsequent interaction with ULF waves that enable the outward radial diffusion of electrons (e.g., Loto'aniu et al., 2010; Rodger et al., 2019). As mentioned above, the NARMAX models do not incorporate the effects of magnetopause shadowing and the use of daily flux averages result imply that such depletions are seen in the forecast values for the following day. After this depletion period, the outer radiation belt is observed to quickly reform, covering a substantially wider radial region from $L^* \sim 2.9$ to the farthest extent of the orbit of the Van Allen Probes ($L^* \sim 5.9$). The simulations show enhancements out beyond $L^* \sim 6.5$. Both simulations show about a day delay before this refilling process begins. This is most probably due to the fact that the forecast models used to calculate the initial electron flux at GEO are currently unable to replicate the rapid emptying and refilling of the radiation belts because the data are averaged over the preceding 24 hr period. Thus, as seen in Figure 7 the electron fluxes at the outer boundary begin to increase about a day later. This is also evident in panels b, c, and e of Figure 8 as the flux levels throughout the outer belt region begin to increase. Table 3 shows the model prediction efficiencies for the two periods under study. The results show that only the case of the fixed coupling method for the quiet period produce a positive PE, indicating that the forecast values are closer to the measured values in comparison to the mean of the measured values. For the other three cases, the use of the mean would provide a more accurate forecast. These values for the PE are smaller than those resulting from the 1 day ahead forecasts PreMevE SubModel 2 (Chen et al., 2019). While the profiles of the VNC fluxes are similar to that measured by MagEIS, their magnitudes differ by a factor 2 or more with the fixed coupling method resulting in values that are more similar to the measured values. The largest differences are seen during the dropout event with the minima in the simulations occurring a day after that observed in the measurements. This time lag is the result of the NARMAX model producing forecasts that represent the average flux values over the previous day. Thus, the reduction in the outer boundary flux used by VERB will exhibit a minimum on the day following the dropout event which would also delay the refilling as well as smoothing out this process over the following day or so. In addition, at the time of the observed flux dropout the simulations clearly show a population of electrons at $L^* = 3$. A similar population may also be seen in the MagEIS measurements shown in panel (d). This effect is clearer when examining cuts through the distributions, as displayed in Figure 9.

Figure 9 shows a comparison of the flux levels resulting from the fixed (blue) and Kp driven (red) coupling methods a function of L^* at various times during the simulations. The green curve represents measurements from MagEIS. The two peaks in the green trace at $L^* \sim 1.5$ and L^* 5–6 represent the inner and outer radiation belt positions. These panels show that during quiet periods (e.g., panel (b)) there is a close correspondence between the simulated and measured flux levels for the outer radiation belt and that the spatial location of the outer belt is fairly well reproduced, resembling the results shown in Figure 6 during the geomagnetically quiet period discussed above. Panel (a) compares the fluxes during the initial part of the simulation when the Kp index indicated a minor geomagnetic storm. While the location of the inner edge of the outer belt from the simulations agrees with the MagEIS measurements, the magnitude and profile of the outer edge do differ with the simulations showing the location of the flux maxima around 1 L^* closer than the measured value. During the electron dropout event (panel c) there is quite a difference in the flux profiles. This may stem from the use of daily averages from the NARMAX forecast models which would result in the fact that these models do not accurately reproduce the sudden loss of electrons at GEO. During the repopulation of the outer belt (panel d) both simulations show reduced levels of fluxes, typically more than an order of magnitude in comparison to the MagEIS measurements. The flux levels generated using the fixed L^* method are greater than those based on the Kp driven coupling method, which arises a direct result of the lower flux levels computed for the VERB outer boundary. Panels (a) and (d) also indicate that the estimation of the fluxes at the VERB outer boundary limit of $L^* = 7$ are also underestimated in comparison with the MagEIS measurements during times of enhanced geomagnetic activity. Closer inspection of the cuts shown in panel (d) show that the increase in the flux levels resulting from the VNC simulations around $L^* = 3$, seen prominently in panels (b) and (c) of Figure 8, actually replicate, to some extent, the observations by MagEIS which reveal a small peak in the population electrons in the region of $L^* = 3$. Thus, this storm appears to have modified the structure of the radiation belts, leading to the creation of a narrow, third
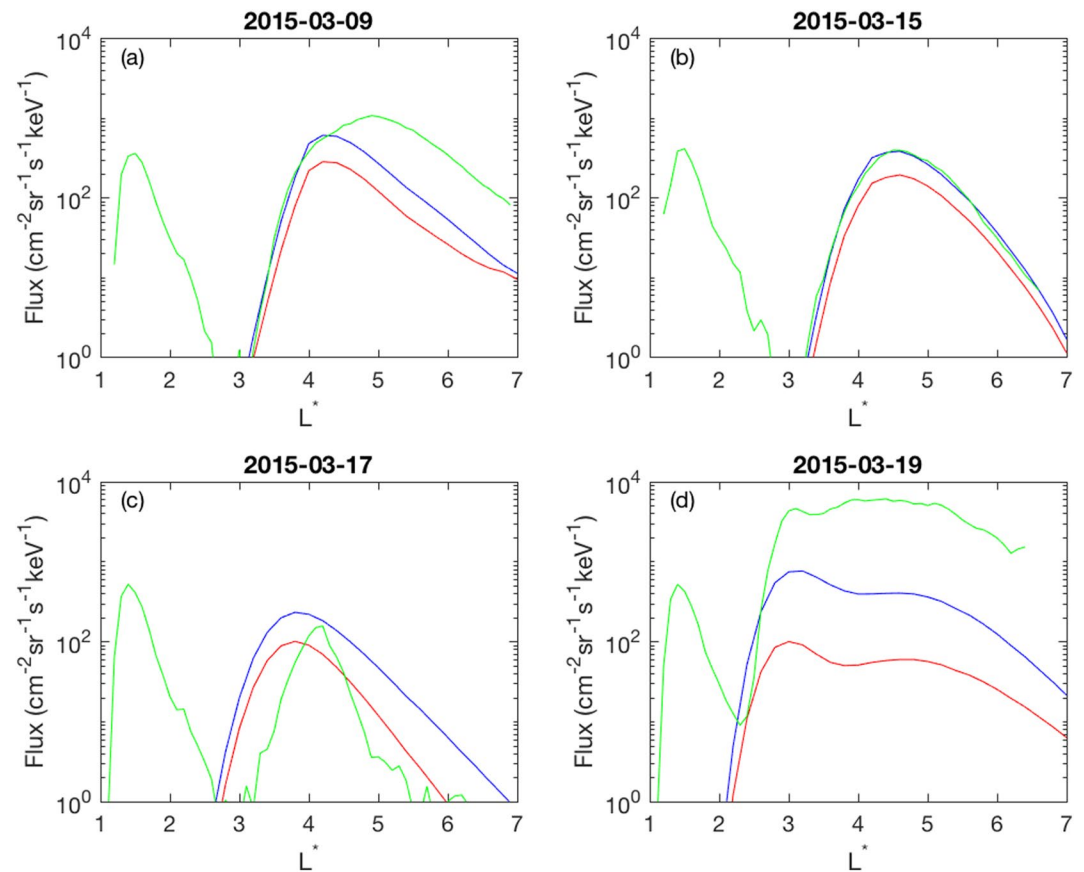
Figure 9. A comparison of the simulated (fixed L^*_{GEO} coupling (blue), variable coupling (red)) and measured (green) fluxes of 0.892 keV electrons as a function of L^*.

belt situated at the inner edge of the outer belt. Longer VNC simulations (not shown) show that this feature lasts until at least mid-June.

Thus, it appears that the use of the Kp driven coupling method does not significantly improve the output from VERB.

7. Summary

In this paper we have investigated the differences in two different coupling schemes used to join the NARMAX generated SNB^{3}GEO models for the fluxes of electrons at GEO with the VERB code to estimate the fluxes of electrons throughout the radiation belt region. The first scheme assumes that the Geostationary Equatorial Orbit lies at a constant radial distance of $L^*_{GEO} = 6.2$ irrespective of geomagnetic activity level. The second scheme computes an average value for L^*_{GEO} based on the current level of geomagnetic activity.

It was shown that the assumption used in the first coupling methodology is only applicable for low values of Kp ($Kp \leq 2$). As Kp increases beyond Kp = 2 the value of L^*_{GEO} begins to deviate from that used in the first coupling methodology. Thus as Kp increases, the value of L^*_{GEO} decreases which then leads to a decrease in flux levels at the VERB outer boundary. The results show that during geomagnetically quiet periods, the difference in computed fluxes using the two coupling methods is small as in panel (e) of Figure 6. During more disturbed times, such as those shown in Figure 8 panel (e) or Figure 9, the difference in flux levels may be as high as a factor 2–3. During the refilling period following the dropout, the Kp driven coupling method yields lower fluxes than the fixed L^*_{GEO} coupling method, possibly up to an order of magnitude. Therefore it appears that this implementation of a Kp driven coupling method does not show any significant advantages. The use of NARMAX flux forecasts with a time resolution of one day severely impairs the VNC model in capturing events with short time durations, such as the flux dropout associated with the 2015 St. Patrick's Day storm and the subsequent repopulation of the

radiation belt environment. We aim to reduce this effect by developing a further suite of NARMAX models to provide forecasts of the electron flux averages with hourly resolution.

Appendix A: Estimation of GEO Electron Flux at a Specific Energy

The SNB^{3}GEO NARMAX models provide 1 day ahead forecasts of the daily averaged electron flux as measured by the integral electron channels (>800 keV and >2 MeV) of the GOES 13 EPAD instrument. In this section the method for the calculation of fluxes at a specific energy is presented. It is based on the method described in Subbotin et al. (2011).

We begin by assuming that the electron distribution within the radiation belts is Maxwellian and maybe expressed as

$$J_E = A \exp(-B * E) \tag{A1}$$

where J_E is the flux at an energy E. A and B are constants of the distribution that need to be determined.

The NARMAX models provide the integral fluxes of particles greater than a lower energy limit, for example,

$$
\begin{aligned}
J(E > E_1) &= \int_{E_1}^{\inf} J(E) \, dE \\
&= \int_{E_1}^{\inf} A \times \exp(-BE) \, dE \\
&= \left[-\frac{A}{B} \exp(-BE) \right]_{E_1}^{\inf} \\
&\approx \frac{A}{B} \exp(-BE)
\end{aligned}
$$

Thus, for the flux J_1 of particles with energies greater than $E_1 = 800$ keV we can write

$$J_1 = \frac{A \exp(-BE_1)}{B} \tag{A2}$$

and similarly for the flux of particles with energies greater than $E_1 = 2,000$ keV

$$J_2 = \frac{A \exp(-BE_2)}{B} \tag{A3}$$

Taking logs and finding the difference in fluxes at energies E_1 and E_2 we find that

$$\log(J_2) - \log(J_1) = -B(E_2 - E_1) \tag{A4}$$

and so the constant B may be determined from

$$\frac{\log\left(\frac{J_2}{J_1}\right)}{(E_2 - E_1)} = -B \tag{A5}$$

Substituting Equation A4 back into Equation A3 and rearranging we can determine A

$$A = \frac{BJ_2}{\exp(-BE_2)}. \tag{A6}$$

Thus, having determined the constants A and B, it is possible to estimate the differential electron flux at a specific energy E based on Equation A1.

Appendix B: Propagation of Electron Flux PSD From GEO to $L^* = 7$

As was mentioned in Section 3, the SNB^{3}GEO models yield forecasts of two integral flux channels at GEO. Section Appendix A outlines the procedure to compute the flux at a specific energy at GEO. GEO lies roughly at $L = 6.6$ and thus the flux requires mapping to $L^* = 7$ so that it can be used to estimate the VERB outer boundary electron flux at $L^* = 7$. The main assumption behind the mapping process is that the particle PSD does not vary

between GEO and the VERB outer boundary limit. Assuming conservation of the first adiabatic invariant the momentum of the electrons of energy E at GEO is calculated using

$$p_{GEO} = \sqrt{\frac{E^2}{c^2} + 2Em_0} \tag{B1}$$

Knowing the flux of particles, the PSD is defined as

$$PSD_{GEO} = \frac{f_{GEO}}{p_{GEO}^2} \tag{B2}$$

and thus in adiabatic invariant is determined using

$$\mu = \frac{p_{GEO}^2 \sin^2(\alpha)}{2m_0 B} \tag{B3}$$

Assuming conservation of PSD from GEO to $L^* = 7$, $PSD_B = PSD_{GEO}$

The particle momentum at the outer boundary is determined bae in the invariant μ and the particle pitch angle

$$p_B = \sqrt{\frac{2\mu m_0 B}{\sin^2(\alpha)}} \tag{B4}$$

Finally, the flux is deduced using

$$f_B = PSD_B p_B^2 \tag{B5}$$

where p, E, m, f, and α are the particle momentum, energy, mass, flux, and pitch angle respectively, at either Geostationary Orbit ($_{GEO}$) or the VERB outer boundary ($_B$), and B the local magnetic field.

The value for the electron flux at the VERB outer boundary is then converted into the scaling factor B_f by interpolating values in Table 2 of Y. Y. Shprits, Subbotin, and Ni (2009). Values of B_f are then used to scale the fluxes that define the boundary condition for the radial diffusion operator used by VERB.

Data Availability Statement

Values for the Kp may be obtained from GFZ, Potsdam, Germany (www.gfz-potsdam.de/kp-index). Van Allen Probes MagEIS data are available from https://rbsp-ect.lanl.gov/data_pub/rbspa/mageis/. The data used to generate the figures are available from https://doi.org/10.15131/shef.data.20079527.

References

Allison, H. J., & Shprits, Y. Y. (2020). Local heating of radiation belt electrons to ultra-relativistic energies. *Nature Communications*, *11*(1), 4533. https://doi.org/10.1038/s41467-020-18053-z

Allison, H. J., Shprits, Y. Y., Zhelavskaya, I. S., Wang, D., & Smirnov, A. G. (2021). Gyroresonant wave-particle interactions with chorus waves during extreme depletions of plasma density in the van Allen radiation belts. *Science Advances*, *7*(5), eabc0380. https://doi.org/10.1126/sciadv.abc0380

Ayala-Solares, J. R., Wei, H. L., Boynton, R. J., Walker, S. N., & Billings, S. A. (2016). Modeling and prediction of global magnetic disturbance in near-Earth space: A case study for Kp index using NARX models. *Space Weather-The International Journal of Research and Applications*, *14*(10), 899–916. https://doi.org/10.1002/2016SW001463

Baker, D. N., Balstad, R., Bodeau, J. M., Cameron, E., Fennell, J. F., Fisher, G. M., et al. (2008). In *Severe space weather events–understanding societal and economic impacts: A workshop report*. The National Academies Press. Tech. Rep. No. 12507. https://doi.org/10.17226/12507

Baker, D. N., McPherron, R. L., Cayton, T. E., & Klebesadel, R. W. (1990). Linear prediction filter analysis of relativistic electron properties at 6.6 RE. *Journal of Geophysical Research*, *95*(A9), 15133–15140. https://doi.org/10.1029/JA095iA09p15133

Balikhin, M. A., Boynton, R. J., Walker, S. N., Borovsky, J. E., Billings, S. A., & Wei, H. L. (2011). Using the NARMAX approach to model the evolution of energetic electrons fluxes at geostationary orbit. *Geophysical Research Letters*, *38*(18), L18105. https://doi.org/10.1029/2011GL048980

Balikhin, M. A., Rodriguez, J. V., Boynton, R. J., Walker, S. N., Aryan, H., Sibeck, D. G., & Billings, S. A. (2016). Comparative analysis of NOAA REFM and SNB3GEO tools for the forecast of the fluxes of high-energy electrons at GEO. *Space Weather*, *14*(1), 22–31. https://doi.org/10.1002/2015SW001303

Beutier, T., & Boscher, D. (1995). A three-dimensional analysis of the electron radiation belt by the salammbô code. *Journal of Geophysical Research*, *100*(A8), 14853–14861. https://doi.org/10.1029/94JA03066

Billings, S. A. (2013). *Nonlinear systems identification: NARMAX, methods in the time, frequency, and spatio-temporal domains*. Wiley-Blackwell.

Billings, S. A., Chen, S., & Korenberg, M. (1989). Identification of MIMO non-linear systems using a foreward-regression orthogonal estimator. *International Journal of Control*, *49*(6), 2157–2189. https://doi.org/10.1080/00207178908961377

Blake, J. B., Carranza, P. A., Claudepierre, S. G., Clemmons, J. H., Crain, W. R., Dotan, Y., et al. (2013). The magnetic electron ion spectrometer (MagEIS) instruments aboard the radiation belt storm probes (RBSP) spacecraft. *Space Science Review*, *179*(1–4), 383–421. https://doi.org/10.1007/s11214-013-9991-8

Boaghe, O., Balikhin, M., Billings, S. A., & Alleyne, H. (2001). Identification of nonlinear processes in the magnetospheric dynamics and forecasting of Dst index. *Journal of Geophysical Research A*, *106*(A12), 30047–30066. https://doi.org/10.1029/2000JA900162

Boberg, F., Wintoft, P., & Lundstedt, H. (2000). Real time Kp predictions from solar wind data using neural networks. *Physics and Chemistry of the Earth*, *25*(4), 275–280. https://doi.org/10.1016/S1464-1917(00)00016-7

Bourdarie, S., & O'Brien, T. P. (2009). International radiation belt environment modelling library. In *COSPAR panel on radiation belt environment modelling (PRBEM) (tech. Rep.)*. ONERA.

Boynton, R. J., Balikhin, M. A., & Billings, S. A. (2015). Online NARMAX model for electron fluxes at GEO. *Annales Geophysicae*, *33*(3), 405–411. https://doi.org/10.5194/angeo-33-405-2015

Boynton, R. J., Balikhin, M. A., Billings, S. A., Reeves, G. D., Ganushkina, N., Gedalin, M., et al. (2013). The analysis of electron fluxes at geosynchronous orbit employing a NARMAX approach. *Journal of Geophysical Research: Space Physics*, *118*(4), 1500–1513. https://doi.org/10.1002/jgra.50192

Boynton, R. J., Balikhin, M. A., Billings, S. A., Wei, H. L., & Ganushkina, N. (2011). Using the NARMAX OLS-ERR algorithm to obtain the most influential coupling functions that affect the evolution of the magnetosphere. *Journal of Geophysical Research*, *116*(A5), A05218. https://doi.org/10.1029/2010JA015505

Boynton, R. J., Balikhin, M. A., Sibeck, D. G., Walker, S. N., Billings, S. A., & Ganushkina, N. (2016). Electron flux models for different energies at geostationary orbit. *Space Weather-The International Journal of Research and Applications*, *14*(10), 846–860. https://doi.org/10.1002/2016SW001506

Brautigam, D. H., & Albert, J. M. (2000). Radial diffusion analysis of outer radiation belt electrons during the October 9, 1990 magnetic storm. *Journal of Geophysical Research A*, *105*(A1), 291–310. https://doi.org/10.1029/1999JA900344

Carpenter, D. L., & Anderson, R. R. (1992). An isee/whistler model of equatorial electron density in the magnetosphere. *Journal of Geophysical Research*, *97*(A2), 1097–1108. https://doi.org/10.1029/91JA01548

Cervantes, S., Shprits, Y. Y., Aseev, N. A., & Allison, H. J. (2020). Quantifying the effects of EMIC wave scattering and magnetopause shadowing in the outer electron radiation belt by means of data assimilation. *Journal of Geophysical Research: Space Physics*, *125*(8), e2020JA028208. https://doi.org/10.1029/2020JA028208

Chen, Y., Reeves, G. D., Fu, X., & Henderson, M. (2019). PreMevE: New predictive model for megaelectron-volt electrons inside Earth's outer radiation belt. *Space Weather*, *17*(3), 438–454. https://doi.org/10.1029/2018SW002095

Claudepierre, S. G., & O'Brien, T. P. (2020). Specifying high-altitude electrons using low-altitude leo systems: The shells model. *Space Weather*, *18*(3), e2019SW002402. https://doi.org/10.1029/2019SW002402

Coca, D., Balikhin, M. A., Billings, S. A., Alleyne, H. S. K., & Dunlop, M. (2001). Time domain analysis of plasma turbulence observed upstream of a quasi-parallel shock. *Journal of Geophysical Research A*, *106*(A11), 25005–25021. https://doi.org/10.1029/2000JA000431

Coleman, T., McCollough, J. P., Young, S., & Rigler, E. J. (2018). Operational nowcasting of electron flux levels in the outer zone of Earth's radiation belt. *Space Weather*, *16*(5), 501–518. https://doi.org/10.1029/2017SW001788

Denton, M. H., Henderson, M. G., Jordanova, V. K., Thomsen, M. F., Borovsky, J. E., Woodroffe, J., et al. (2016). An improved empirical model of electron and ion fluxes at geosynchronous orbit based on upstream solar wind conditions. *Space Weather*, *14*(7), 511–523. https://doi.org/10.1002/2016SW001409

Drozdov, A. Y., Shprits, Y. Y., Orlova, K. G., Kellerman, A. C., Subbotin, D. A., Baker, D. N., et al. (2015). Energetic, relativistic, and ultrarelativistic electrons: Comparison of long-term verb code simulations with van Allen probes measurements. *Journal of Geophysical Research: Space Physics*, *120*(5), 3574–3587. https://doi.org/10.1002/2014JA020637

Drozdov, A. Y., Shprits, Y. Y., Usanova, M. E., Aseev, N. A., Kellerman, A. C., & Zhu, H. (2017). EMIC wave parameterization in the long-term VERB code simulation. *Journal of Geophysical Research: Space Physics*, *122*(8), 8488–8501. https://doi.org/10.1002/2017JA024389

Drozdov, A. Y., Usanova, M. E., Hudson, M. K., Allison, H. J., & Shprits, Y. Y. (2020). The role of hiss, chorus, and EMIC waves in the modeling of the dynamics of the multi-MeV radiation belt electrons. *Journal of Geophysical Research: Space Physics*, *125*(9), e2020JA028282. https://doi.org/10.1029/2020JA028282

Dungey, J. W. (1965). Effects of electromagnetic perturbations on particles trapped in the radiation belts. *Space Science Review*, *4*(2), 199–222. https://doi.org/10.1007/BF00173882

Fok, M.-C., Horne, R. B., Meredith, N. P., & Glauert, S. A. (2008). Radiation belt environment model: Application to space weather nowcasting. *Journal of Geophysical Research: Space Physics*, *113*(A12), 3. https://doi.org/10.1029/2007JA012558

Fukata, M., Taguchi, S., Okuzawa, T., & Obara, T. (2002). Neural network prediction of relativistic electrons at geosynchronous orbit during the storm recovery phase: Effects of recurring substorms. *Annales Geophysicae*, *20*(7), 947–951. https://doi.org/10.5194/angeo-20-947-2002

Ganushkina, N. Y., Swiger, B., Dubyagin, S., Matéo-Vélez, J.-C., Liemohn, M. W., Sicard, A., & Payan, D. (2021). Worst-case severe environments for surface charging observed at LANL satellites as dependent on solar wind and geomagnetic conditions. *Space Weather*, *19*(9), e2021SW002732. https://doi.org/10.1029/2021SW002732

Ginet, G. P., O'Brien, T. P., Huston, S. L., Johnston, W. R., Guild, T. B., Friedel, R., et al. (2013). AE9, AP9 and SPM: New models for specifying the trapped energetic particle and space plasma environment. *Space Science Review*, *179*(1), 579–615. https://doi.org/10.1007/s11214-013-9964-y

Glauert, S. A., Horne, R. B., & Kirsch, P. (2021). Evaluation of SaRIF high-energy electron reconstructions and forecasts. *Space Weather*, *19*(12), e2021SW002822. https://doi.org/10.1029/2021SW002822

Glauert, S. A., Horne, R. B., & Meredith, N. P. (2014a). Simulating the Earth's radiation belts: Internal acceleration and continuous losses to the magnetopause. *J. Journal of Geophysical Research: Space Physics*, *119*(9), 7444–7463. https://doi.org/10.1002/2014JA020092

Glauert, S. A., Horne, R. B., & Meredith, N. P. (2014b). Three-dimensional electron radiation belt simulations using the BAS radiation belt model with new diffusion models for chorus, plasmaspheric hiss, and lightning-generated whistlers. *Journal of Geophysical Research: Space Physics*, *119*(1), 268–289. https://doi.org/10.1002/2013JA019281

Goldstein, J., Angelopoulos, V., De Pascuale, S., Funsten, H. O., Kurth, W. S., Llera, K., et al. (2017). Cross-scale observations of the 2015 St. Patrick's Day storm: THEMIS, van Allen probes, and TWINS. *Journal of Geophysical Research: Space Physics*, *122*(1), 368–392. https://doi.org/10.1002/2016JA023173

Green, J. C., Likar, J., & Shprits, Y. (2017). Impact of space weather on the satellite industry. *Space Weather*, *15*(6), 804–818. https://doi.org/10.1002/2017SW001646

Green, J. C., Onsager, T. G., O'Brien, T. P., & Baker, D. N. (2004). Testing loss mechanisms capable of rapidly depleting relativistic electron flux in the Earth's outer radiation belt. *Journal of Geophysical Research: Space Physics*, *109*(A12), A12211. https://doi.org/10.1029/2004JA010579

Hanser, F. A. (2011). *EPS/HEPAD calibration and data handbook (Tech. Rep. No. GOESN-ENG-048D). Carlisle, Mass.* Assurance Technol. Corp.

Herrera, D., Maget, V. F., & Sicard-Piet, A. (2016). Characterizing magnetopause shadowing effects in the outer electron radiation belt during geomagnetic storms. *Journal of Geophysical Research: Space Physics*, *121*(10), 9517–9530. https://doi.org/10.1002/2016JA022825

Heynderickx, D., Quaghebeur, B., Wera, J., Daly, E. J., & Evans, H. D. R. (2004). New radiation environment and effects models in the European Space Agency's Space Environment Information System (SPENVIS). *Space Weather*, *2*(10), S10S03. https://doi.org/10.1029/2004SW000073

Horne, R. B., & Thorne, R. M. (1998). Potential waves for relativistic electron scattering and stochastic acceleration during magnetic storms. *Geophysical Research Letters*, *25*(15), 3011–3014. https://doi.org/10.1029/98GL01002

Horne, R. B., Thorne, R. M., Glauert, S. A., Albert, J. M., Meredith, N. P., & Anderson, R. R. (2005). Timescale for radiation belt electron acceleration by whistler mode chorus waves. *Journal of Geophysical Research*, *110*(A3), A03225. https://doi.org/10.1029/2004JA010811

Jaynes, A. N., Baker, D. N., Singer, H. J., Rodriguez, J. V., Loto'aniu, T. M., Ali, A. F., et al. (2015). Source and seed populations for relativistic electrons: Their roles in radiation belt changes. *Journal of Geophysical Research: Space Physics*, *120*(9), 7240–7254. https://doi.org/10.1002/2015JA021234

Kennel, C. F. (1969). Consequences of a magnetospheric plasma. *Reviews of Geophysics*, *7*(1–2), 379–419. https://doi.org/10.1029/RG007i001p00379

Koller, J., & Zaharia, S. (2011). Lanl*v2.0: Global modeling and validation. *Geoscientific Model Development*, *4*(3), 669–675. https://doi.org/10.5194/gmd-4-669-2011

Konstantinidis, K., & Sarris, T. (2015). Calculations of the integral invariant coordinates i and l* in the magnetosphere and mapping of the regions where i is conserved, using a particle tracer (ptr3d v2.0), LANL*, SPENVIS, and IRBEM. *Geoscientific Model Development*, *8*(9), 2967–2975. https://doi.org/10.5194/gmd-8-2967-2015

Lenchek, A. M., Singer, S. F., & Wentworth, R. C. (1961). Geomagnetically trapped electrons from cosmic ray albedo neutrons. *Journal of Geophysical Research (1896-1977)*, *66*(12), 4027–4046. https://doi.org/10.1029/JZ066i012p04027

Leontaritis, I., & Billings, S. A. (1985a). Input-output parametric models for nonlinear systems, Part I: Deterministic nonlinear systems. *International Journal of Control*, *41*(2), 309–328. https://doi.org/10.1080/0020718508961129

Leontaritis, I., & Billings, S. A. (1985b). Input-output parametric models for nonlinear systems, Part II: Stochastic nonlinear systems. *International Journal of Control*, *41*(2), 329–344. https://doi.org/10.1080/0020718508961130

Li, W., Shprits, Y. Y., & Thorne, R. M. (2007). Dynamic evolution of energetic outer zone electrons due to wave-particle interactions during storms. *Journal of Geophysical Research*, *112*(A10), A10220. https://doi.org/10.1029/2007JA012368

Li, W., Thorne, R. M., Ma, Q., Ni, B., Bortnik, J., Baker, D. N., et al. (2014). Radiation belt electron acceleration by chorus waves during the 17 March 2013 storm. *Journal of Geophysical Research: Space Physics*, *119*(6), 4681–4693. https://doi.org/10.1002/2014JA019945

Li, X., Baker, D. N., Temerin, M., Cayton, T. E., Reeves, G. D., Christensen, R. A., et al. (1997). Multisatellite observations of the outer zone electron variation during the November 3–4, 1993, magnetic storm. *Journal of Geophysical Research*, *102*(A7), 14123–14140. https://doi.org/10.1029/97JA01101

Loto'aniu, T. M., Singer, H. J., Waters, C. L., Angelopoulos, V., Mann, I. R., Elkington, S. R., & Bonnell, J. W. (2010). Relativistic electron loss due to ultralow frequency waves and enhanced outward radial diffusion. *Journal of Geophysical Research*, *115*(A12), A12245. https://doi.org/10.1029/2010JA015755

Lyons, L. R., & Thorne, R. M. (1972). Parasitic pitch angle diffusion of radiation belt particles by ion cyclotron waves. *Journal of Geophysical Research*, *77*(28), 5608–5616. https://doi.org/10.1029/JA077i028p05608

McIlwain, C. E. (1961). Coordinates for mapping the distribution of magnetically trapped particles. *Journal of Geophysical Research (1896-1977)*, *66*(11), 3681–3691. https://doi.org/10.1029/JZ066i011p03681

Meredith, N. P., Horne, R. B., Glauert, S. A., & Anderson, R. R. (2007). Slot region electron loss timescales due to plasmaspheric hiss and lightning-generated whistlers. *Journal of Geophysical Research*, *112*(A8), 8214. https://doi.org/10.1029/2007JA012413

Meredith, N. P., Horne, R. B., Isles, J. D., & Rodriguez, J. V. (2015). Extreme relativistic electron fluxes at geosynchronous orbit: Analysis of GOES E > 2 MeV electrons. *Space Weather*, *13*(3), 170–184. https://doi.org/10.1002/2014SW001143

Nagai, T. (1988). Space weather forecast: Prediction of relativistic electron intensity at synchronous orbit. *Geophysical Research Letters*, *15*(5), 425–428. https://doi.org/10.1029/GL015i005p00425

Pakhotin, I. P., Drozdov, A. Y., Shprits, Y. Y., Boynton, R. J., Subbotin, D. A., & Balikhin, M. A. (2014). Simulation of high-energy radiation belt electron fluxes using NARMAX-VERB coupled codes. *Journal of Geophysical Research: Space Physics*, *119*(10), 8073–8086. https://doi.org/10.1002/2014JA020238

Rastätter, L., Kuznetsova, M. M., Glocer, A., Welling, D., Meng, X., Raeder, J., et al. (2013). Geospace environment modeling 2008–2009 challenge: Dst index. *Space Weather*, *11*(4), 187–205. https://doi.org/10.1002/swe.20036

Reeves, G. D., Chen, Y., Cunningham, G. S., Friedel, R. W. H., Henderson, M. G., Jordanova, V. K., et al. (2012). Dynamic radiation environment assimilation model: Dream. *Space Weather*, *10*(3), S03006. https://doi.org/10.1029/2011SW000729

Reeves, G. D., McAdams, K. L., Friedel, R. H. W., & O'Brien, T. P. (2003). Acceleration and loss of relativistic electrons during geomagnetic storms. *Geophysical Research Letters*, *30*(10), 1529. https://doi.org/10.1029/2002GL016513

Reeves, G. D., Morley, S. K., Friedel, R. H. W., Henderson, M. G., Cayton, T. E., Cunningham, G., et al. (2011). On the relationship between relativistic electron flux and solar wind velocity: Paulikas and blake revisited. *Journal of Geophysical Research*, *116*(A2), A02213. https://doi.org/10.1029/2010JA015735

Ripoll, J.-F., Claudepierre, S. G., Ukhorskiy, A. Y., Colpitts, C., Li, X., Fennell, J. F., & Crabtree, C. (2020). Particle dynamics in the Earth's radiation belts: Review of current research and open questions. *Journal of Geophysical Research: Space Physics*, *125*(5), e2019JA026735. https://doi.org/10.1029/2019JA026735

Rodger, C. J., Turner, D. L., Clilverd, M. A., & Hendry, A. T. (2019). Magnetic local time-resolved examination of radiation belt dynamics during high-speed solar wind speed-triggered substorm clusters. *Geophysical Research Letters*, *46*(17–18), 10219–10229. https://doi.org/10.1029/2019GL083712

Roederer, J. G. (1970). *Dynamics of geomagnetically trapped radiation*. Springer-Verlag.

Roederer, J. G., & Lejosne, S. (2018). Coordinates for representing radiation belt particle flux. *Journal of Geophysical Research: Space Physics*, *123*(2), 1381–1387. https://doi.org/10.1002/2017JA025053

Schultz, M., & Lanzerotti, L. J. (1974). *Particle diffusion in the radiation belts* (Vol. 7). Springer-Verlag.

Sheeley, B. W., Moldwin, M. B., Rassoul, H. K., & Anderson, R. R. (2001). An empirical plasmasphere and trough density model: CRRES observations. *Journal of Geophysical Research A*, *106*(A11), 25631–25642. https://doi.org/10.1029/2000JA000286

Shin, D.-K., Lee, D.-Y., Kim, K.-C., Hwang, J., & Kim, J. (2016). Artificial neural network prediction model for geosynchronous electron fluxes: Dependence on satellite position and particle energy. *Space Weather*, *14*(4), 313–321. https://doi.org/10.1002/2015SW001359

Shprits, Y., Kellerman, A., Kondrashov, D., & Subbotin, D. (2013). Application of a new data operator-splitting data assimilation technique to the 3-D VERB diffusion code and CRRES measurements. *Geophysical Research Letters*, *40*(19), 4998–5002. https://doi.org/10.1002/grl.50969

Shprits, Y., Kondrashov, D., Chen, Y., Thorne, R., Ghil, M., Friedel, R., & Reeves, G. (2007). Reanalysis of relativistic radiation belt electron fluxes using CRRES satellite data, a radial diffusion model, and a Kalman filter. *Journal of Geophysical Research*, *112*(A12), A12216. https://doi.org/10.1029/2007JA012579

Shprits, Y. Y., Chen, L., & Thorne, R. M. (2009). Simulations of pitch angle scattering of relativistic electrons with MLT-dependent diffusion coefficients. *Journal of Geophysical Research*, *114*(A3), A03219. https://doi.org/10.1029/2008JA013695

Shprits, Y. Y., Kellerman, A. C., Drozdov, A. Y., Spence, H. E., Reeves, G. D., & Baker, D. N. (2015). Combined convective and diffusive simulations: VERB-4D comparison with 17 March 2013 van Allen probes observations. *Geophysical Research Letters*, *42*(22), 9600–9608. https://doi.org/10.1002/2015GL065230

Shprits, Y. Y., Subbotin, D., & Ni, B. (2009). Evolution of electron fluxes in the outer radiation belt computed with the VERB code. *Journal of Geophysical Research*, *114*(A13), 11209. https://doi.org/10.1029/2008JA013784

Shprits, Y. Y., Subbotin, D. A., Meredith, N. P., & Elkington, S. R. (2008). Review of modeling of losses and sources of relativistic electrons in the outer radiation belt i: Local acceleration and loss. *Journal of Atmospheric and Solar-Terrestrial Physics*, *70*(14), 1694–1713. https://doi.org/10.1016/j.jastp.2008.06.014

Shprits, Y. Y., & Thorne, R. M. (2004). Time dependent radial diffusion modeling of relativistic electrons with realistic loss rates. *Geophysical Research Letters*, *31*(8), L08805. https://doi.org/10.1029/2004GL019591

Shprits, Y. Y., Thorne, R. M., Friedel, R., Reeves, G. D., Fennell, J., Baker, D. N., & Kanekal, S. G. (2006). Outward radial diffusion driven by losses at magnetopause. *Journal of Geophysical Research*, *111*(A11), A11214. https://doi.org/10.1029/2006JA011657

Smirnov, A. G., Berrendorf, M., Shprits, Y. Y., Kronberg, E. A., Allison, H. J., Aseev, N. A., et al. (2020). Medium energy electron flux in Earth's outer radiation belt (MERLIN): A machine learning model. *Space Weather*, *18*(11), e2020SW002532. https://doi.org/10.1029/2020SW002532

Staples, F. A., Kellerman, A., Murphy, K. R., Rae, I. J., Sandhu, J. K., & Forsyth, C. (2022). Resolving magnetopause shadowing using multi-mission measurements of phase space density. *Journal of Geophysical Research: Space Physics*, *127*(2), e2021JA029298. https://doi.org/10.1029/2021JA029298

Stratton, J. M., Harvey, R. J., & Heyler, G. A. (2013). Mission overview for the radiation belt storm probes mission. *Space Science Reviwew*, *179*(1–4), 29–57. https://doi.org/10.1007/s11214-012-9933-x

Subbotin, D. A., & Shprits, Y. Y. (2009). Three-dimensional modeling of the radiation belts using the versatile electron radiation belt (VERB) code. *Space Weather*, *7*(10), S10001. https://doi.org/10.1029/2008SW000452

Subbotin, D. A., Shprits, Y. Y., & Ni, B. (2011). Long-term radiation belt simulation with the VERB 3-D code: Comparison with CRRES observations. *Journal of Geophysical Research*, *116*(A15), 12210. https://doi.org/10.1029/2011JA017019

Temerin, M., & Li, X. (2006). Dst model for 1995-2002. *Journal of Geophysical Research (1896-1977)*, *111*(A4), A4221. https://doi.org/10.1029/2005JA011257

Thorne, R. M., Smith, E. J., Fiske, K. J., & Church, S. R. (1974). Intensity variation of elf hiss and chorus during isolated substorms. *Geophysical Research Letters*, *1*(5), 193–196. https://doi.org/10.1029/GL001i005p00193

Tsyganenko, N. A. (1989). A magnetospheric magnetic field model with a warped tail current sheet. *Planetary and Space Science*, *37*(1), 5–20. https://doi.org/10.1016/0032-0633(89)90066-4

Tu, W., Cunningham, G. S., Chen, Y., Henderson, M. G., Camporeale, E., & Reeves, G. D. (2013). Modeling radiation belt electron dynamics during gem challenge intervals with the dream 3d diffusion model. *Journal of Geophysical Research: Space Physics*, *118*(10), 6197–6211. https://doi.org/10.1002/jgra.50560

Vampola, A. L. (1992). Combined release and radiation effects satellite. *Journal of Spacecraft and Rockets*, *29*(4), 555. https://doi.org/10.2514/3.55640

Van Allen, J. A., & Frank, L. A. (1959). Radiation around the Earth to a radial distance of 107, 400 km. *Nature*, *183*(4659), 430–434. https://doi.org/10.1038/183430a0

Varotsou, A., Boscher, D., Bourdarie, S., Horne, R. B., Meredith, N. P., Glauert, S. A., & Friedel, R. H. (2008). Three-dimensional test simulations of the outer radiation belt electron dynamics including electron-chorus resonant interactions. *Journal of Geophysical Research*, *113*(A12), A12212. https://doi.org/10.1029/2007JA012862

Wing, S., Johnson, J. R., Jen, J., Meng, C.-I., Sibeck, D. G., Bechtold, K., et al. (2005). Kp forecast models. *Journal of Geophysical Research*, *110*(A4), 4203. https://doi.org/10.1029/2004JA010500

Wintoft, P., Wik, M., Matzka, J., & Shprits, Y. (2017). Forecasting Kp from solar wind data: Input parameter study using 3-hour averages and 3-hour range values. *Journal of Space Weather and Space Climate*, *7*(27), A29. https://doi.org/10.1051/swsc/2017027

Wrenn, G. L., Rodgers, D. J., & Ryden, K. A. (2002). A solar cycle of spacecraft anomalies due to internal charging. *Annales Geophysicae*, *20*(7), 953–956. https://doi.org/10.5194/angeo-20-953-2002

Wu, C.-C., Liou, K., Lepping, R. P., Hutting, L., Plunkett, S., Howard, R. A., & Socker, D. (2016). The first super geomagnetic storm of solar cycle 24: The St. Patrick's Day event (17 March 2015). *Earth Planets and Space*, *68*(1), 151. https://doi.org/10.1186/s40623-016-0525-y

Zhang, S.-R., Zhang, Y., Wang, W., & Verkhoglyadova, O. P. (2017). Geospace system responses to the St. Patrick's Day storms in 2013 and 2015. *Journal of Geophysical Research: Space Physics*, *122*(6), 6901–6906. https://doi.org/10.1002/2017JA024232